U.PORTO
FACULDADE DE CIÊNCIAS
UNIVERSIDADE DO PORTO

MSc

MSc

2.º
CICLO

FCUP
2020

U.PORTO

The Nature of Leo T Ultra-Faint Dwarf

Daniel André Dias Vaz

FC

U.PORTO
FACULDADE DE CIÊNCIAS
UNIVERSIDADE DO PORTO

MSc

The Nature of Leo T Ultra-Faint Dwarf

Daniel André Dias Vaz
Dissertação de Mestrado apresentada à
Faculdade de Ciências da Universidade do Porto em
Astronomia e Astrofísica

2020

MSc

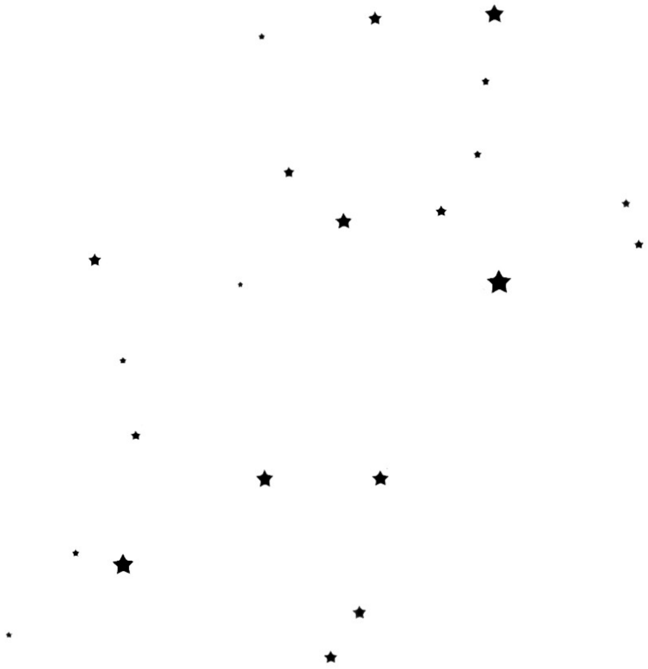

The Nature of Leo T Ultra-Faint Dwarf

Daniel André Dias Vaz
Mestrado em Astronomia e Astrofísica
Departamento de Física e Astronomia
2020

Orientador
Jarle Brinchmann, Investigador,
Instituto de Astrofísica e Ciências do Espaço

U.PORTO

FC FACULDADE DE CIÊNCIAS
UNIVERSIDADE DO PORTO

Todas as correções determinadas pelo júri, e só essas, foram efetuadas.

O Presidente do Júri,

Porto, ______/______/_________

MSc

Agradecimentos

Primeiro de tudo, o meu agradecimento mais especial vai para o Dr. Jarle Brinchmann. Foi uma honra e uma fantástica experiência tê-lo como meu orientador durante este último ano. Agradeço-lhe todo o tempo que despendeu comigo e, acima de tudo, a disponibilidade e prontidão com que sempre me ajudou e orientou nos momentos mais complicados deste projecto. Agradeço toda a experiência e conhecimento que partilhou e que, aliado ao seu positivismo, me motivou especialmente nos momentos mais díficeis, num ano em que nada foi fácil. Por tudo isto e muito mais, o meu mais sincero agradecimento.

Quero agradecer a todos os elementos do MUSE Consortium cujo trabalho permitiu a realização deste projecto. Em especial, agradeço ao Bas Zountendijk pela disponibilidade e enorme ajuda que me deu, e que, sem a qual, o resultado final deste projecto não seria o mesmo.

Um agradecimento a todos os professores da FCUP que me acompanharam ao longo desta caminhada, com menção especial à directora do Mestrado em Astronomia e Astrofísica, professora Dr. Catarina Lobo, por todo o apoio e ajuda que me deu, determinante no ínicio desta etapa.

Por fim, um especial obrigado à minha família e amigos, por todos os bons momentos que me proporcionaram e pela força e carinho que sempre demonstraram.

A todos os que contribuíram para a realização deste trabalho, o meu obrigado.

Resumo

A galáxia anã ultra-fraca chamada Leo T (Irwin et al., 2007) é uma das galáxias mais pequenas, menos brilhantes e mais dominadas por matéria escura, actualmente conhecidas. É, também, uma das mais distantes galáxias satélite da Via Láctea. Estudos existentes sobre galáxias ultra-fracas (Simon, 2019) mostram que o seus rácios massa dinâmica/luminosidade são os valores mais altos medidos para qualquer tipo de galáxia. Isto implica a existência de halos de matéria escura relativamente pura, com mínima matéria bariónica. Esta combinação de características faz de Leo T um laboratório extremamente valioso para restringir a natureza da matéria escura. Para além disso, é conhecido que as galáxias ultra-fracas são as galáxias mais velhas, mais pequenas e com menor metalicidade e massa estelar. As suas histórias de formação são também as mais simples de todas as galáxias estudadas até hoje. Estudos teóricos e observacionais indicam que estas galáxias formaram-se antes da época de reionização e sofreram pouca ou nenhuma evolução depois da sua formação. Entender a natureza destas galáxias iria aumentar imensamente o conhecimento sobre o processo de formação de galáxias. Contudo, todo este potencial tem um preço: a luminosidade extremamente baixa das galáxias ultra-fracas torna a tarefa de estudar as suas estrelas bastante difícil.

Nesta dissertação é discutido um novo estudo da galáxia Leo T, efetuado usando dados do espectrógrafo de campo integral MUSE (Bacon et al., 2010). A alta sensibilidade do espectrógrafo MUSE permitiu obter medições de velocidade para estrelas com magnitudes até ~ 24. Isto permitiu aumentar o número de estrelas pertencente a Leo T espectroscopicamente observadas de 19 para 75. Dentro desta amostra foram descobertas três estrelas que apresentam riscas de emissão - as primeiras em anãs ultra-fracas. Foi realizada uma análise da dinâmica de Leo T, de forma a restringir o seu perfil de densidade. Modelando a dinâmica, foi derivado o primeiro perfil de densidade de matéria escura de Leo T. Este perfil não parece mostrar um núcleo, como observado em anãs mais massivas, mas é consistente com o perfil esperado pelos modelos de matéria escura fria. Combinando os dados do espectrógrafo MUSE com dados fotométricos provenientes do telescópio espacial Hubble, também foi estudada a idade e metalicidade das estrelas, procurando diferenças na dinâmica das estrelas novas e velhas.

Abstract

Leo T Ultra-Faint Dwarf (UFD) (Irwin et al., 2007) is one of the smallest, faintest and most dark matter-dominated galaxies currently known. It is also one of the most distant Milky Way Satellite galaxies known to date. Previous studies of UFDs (Simon, 2019) show that their dynamical mass-to–light ratios are the highest values measured in any type of galaxy, which implies relatively pure dark-matter halos with minimal baryonic content. This combination of characteristics makes Leo T an extremely valuable laboratory for constraining the nature of dark matter. Furthermore, UFDs have the lowest metallicities, oldest ages, smallest sizes, smallest stellar masses, and simplest assembly histories of all galaxies. Observations and theoretical studies indicate that these galaxies formed before the epoch of reionization and have undergone almost no evolution after their formation. Understanding the nature of these galaxies would immensely improve the knowledge of the galaxy formation process. However, all this raw potential comes at a price: the extremely low luminosity of UFDs makes the task of studying their stars quite difficult.

In this dissertation a novel study of Leo T is presented, using data from the MUSE integral field spectrograph (Bacon et al., 2010). The high sensitivity of MUSE has allowed us to obtain velocity measurements for stars as faint as magnitude ~ 24. This has allowed us to increase the number of spectroscopically observed Leo T stars from 19 to 75. Within this sample it was discovered three emission lines stars - a first for ultra-faint dwarfs. Based on these data, an analysis of the dynamics of Leo T was carried out to constrain its dark matter profile. By modelling the dynamics, it was derived the first ever dark matter density profile of the dwarf, which does not appear to show a core like massive dwarfs, but is rather more consistent with a profile expected from cold dark matter models. Combining the MUSE data with photometric data from HST, it was also studied the age and metallicity of the stars, while looking for differences in the dynamics of young and old stars.

Contents

List of Figures

List of Tables

Chapter 1.

Introduction

1.1 How small can a small galaxy be?

For tens of thousands of years, human beings have been looking to the sky, fascinated by the patterns of the stars and wondering what mysteries lurk behind the glamorous festival of lights. Early astronomers quickly concluded that such beauty and complexity could only be caused by manifestations of the divine. Naturally, the knowledge about celestial bodies grew with the evolution of mankind and, today, many secrets of the universe have been demystified.

Nevertheless, today's astronomers continue to look up, still mesmerized and with more questions than ever. Some of these questions are more trivial than others, but one that quickly comes to mind is how small can the smallest galaxy be. To answer this question, a relentless search for the smallest and faintest galaxy ever known has been carried out. As more data became available, it was discovered what are now known as the classical dwarf spheroidal (dSph) satellites of the Milky Way. However, due to limitations in technology, the search for smaller and fainter galaxies continued fruitlessly for many years, even though there were strong theoretical reasons to expect that substantially smaller galaxies with lower luminosities and surface brightnesses should exist (Simon, 2019).

Prior to 2004, the smallest galaxy known was Draco, with a stellar mass of $M_\star \approx 5 \times 10^5 M_\odot$ and absolute magnitude of $M_V = -8.8$ (Mateo, 1998). Today, there are known galaxies 1000 times less luminous (Bullock and Boylan-Kolchin, 2017). The advent of wide-field digital sky surveys with deep exposures and accurate star separation algorithms has revolutionized the search for and discovery of faint galaxies. Distinctively, in 2005, the first of such objects discovered with **S**loan **D**igital **S**ky **S**urvey (SDSS) opened the floodgates, and within two years the known population of Milky Way satellite galaxies more than doubled (Simon, 2019). In Fig. 1.1 is shown a historical perspective that clearly highlights the impact on the discovery of Milky Way satellite galaxies with the emergence of SDSS (from 2005-2010) and DES/Pan-STARRS (2015).

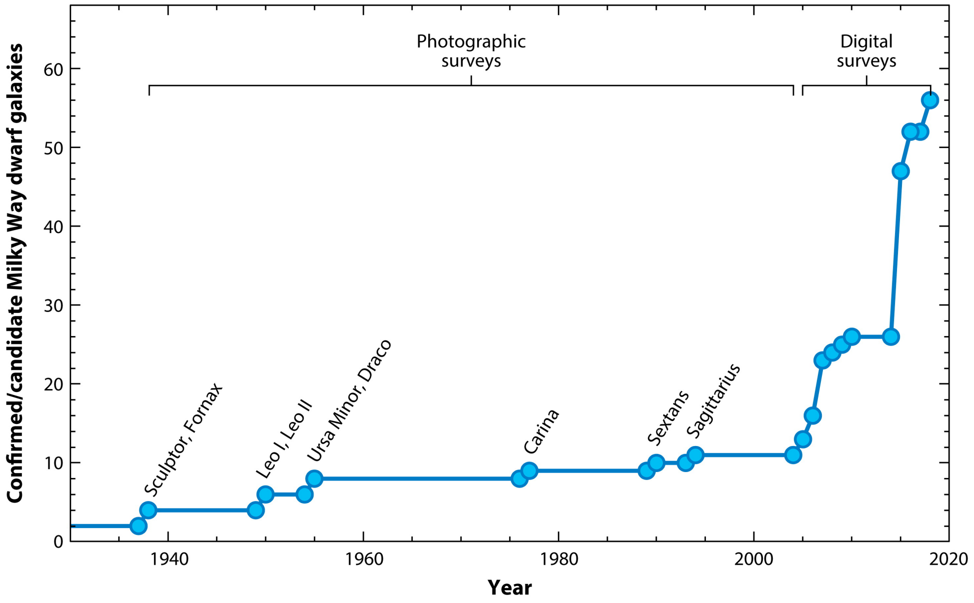

Simon JD. 2019.
Annu. Rev. Astron. Astrophys. 57:375–415

Figure 1.1: Census of Milky Way satellite galaxies as a function of time. The objects shown here include all confirmed dwarf galaxies as well as those suspected to be dwarfs based on less conclusive spectroscopic and photometric measurements.

Within this dwarf population, some galaxies stand out for being fainter and smaller than others. For these is common usage to call them **U**ltra-**F**aint **D**warf**s** (UFDs).

1.2 What is an Ultra-Faint Dwarf?

As discussed above, the dwarf galaxies known prior to 2005 are brighter than $M_V = -8.8$. With the discovery of dwarfs 1000 times less luminous, with half-light radii as small as $\approx 20pc$ and surface brightnesses 3 $mag\ arcsec^{-2}$ fainter than ever before, the community rapidly began referring to these objects as **U**ltra-**F**aint **D**warf**s** (UFDs). Even though they are not a physically distinct class of objects, there are several reasons why it is useful to refer to them independently. In particular, UFDs are the smallest and faintest galaxies currently known. They represent the extreme end of galaxy properties distribution. Previous studies of UFDs show that their dynamical mass-to–light ratios are the highest values measured in any type of galaxy, which implies relatively pure dark-matter halos with minimal baryonic content. Furthermore, UFDs have the lowest metallicities, oldest ages, smallest sizes, smallest stellar masses, and simplest assembly histories of all galaxies. Observations and theoretical studies indicate that these galaxies formed before the epoch of reionization and have undergone almost no evolution after their formation.

Therefore, even though they are the most inconspicuous galaxies ever formed, these systems are critical objects to understand, with potentially wide-ranging implications. As UFDs are the most dark matter-dominated systems known and have survived to the present day as pristine relics from the early universe, they are, not only, an extremely valuable laboratory for constraining the nature of dark matter, but also a window to study the conditions at the time when the first galaxies were forming.

1.3 Dark Matter in Ultra-Faint Dwarfs

The nature of **D**ark **M**atter (DM) is one of the most puzzling questions in astrophysics, and UFDs are the perfect candidates to provide insight into it. Because they are the most DM dominated systems known and due to their small sizes, they offer probes of dark matter on smaller scales. As they are the closest dark matter halos to us and because their internal dynamics are so gentle that heating by very weak effects is potentially measurable, UFDs have attracted a great deal of attention from a broad cross-section of astrophysicists, which can facilitate indirect detection of dark matter. Besides that, it should be possible to measure the inner density profile of a highly dark matter-dominated system using an UFD. Their disadvantage is that they contain so few stars that there may not be enough dynamical tracers for a robust measurement of the mass distribution.

In this context, the Λ **C**old **D**ark **M**atter (ΛCDM) model of cosmology gives a remarkable description of the large-scale structure of the Universe and basic properties of galaxies that form within dark matter halos. However, on smaller scales, i.e. collapsed objects with $M \leq 10^{11}\ M_{\odot}$

(Bullock and Boylan-Kolchin, 2017), there have been long-standing tensions (Read, Walker, and Steger, 2019), the oldest of these beeing the *cusp-core* problem.

Using N-body simulations, it is predicted that internal structure of a dark matter halo should not follow a simple power-law, but a profile that has a dense *cusp* at the center, with inner density obeying $\rho(r) \propto r^{\alpha}$ at small radii, with $\alpha \sim -1.4 \ to \ -0.8$. By contrast, many low-mass dark-matter-dominated galaxies with well measured rotation curves prefer fits with constant-density cores, with $\alpha \sim -0.5 \ to \ 0$ at small radii. Simulations have now progressed to a point that a fairly robust understanding of the structure of ΛCDM halos exists, at least, for dark-matter-only simulations. It is common, in a first approximation, to describe dark matter halo profiles by using a nearly universal form over all masses, with a steep fall-off at large radii, transitioning to mildly divergent cusp towards the center (Bullock and Boylan-Kolchin, 2017). To this end, the NFW functional form (Navarro, Frenk, and White, 1997) provides a good description of dark matter profiles:

$$\rho_{NFW}(r) = \rho_0 \left(\frac{r}{r_s}\right)^{-1} \left(1 + \frac{r}{r_s}\right)^{-2}, \tag{1.1}$$

where ρ_0 is the central density, and r_s is the scale length which marks the transition point from the inner cusp to an outer profile.

The *cusp-core* problem has generated substantial interest over the past two decades. Many solutions has been proposed to this problem, with the currently most accepted claiming that, if gas is slowly accreted onto a dwarf and suddenly removed by the action of stellar winds or supernovae feedback, the DM halo should expand, lowering its central density and creating a core. One key prediction is that the effect of core creation will vary with the number of stars formed. If galaxies form enough stars, there will be enough energy to redistribute dark matter and create significant cores. On the other end, if too few stars are formed, it will be not sufficient to alter halo density structure and the resultant dark matter distribution will resemble dark-matter-only simulations. There is also evidence that even low-level star formation repeated over several cycles can have an accumulated effect that leads to dark matter core formation. This behavior is illustrated in Figure 1.2 (Bullock and Boylan-Kolchin, 2017), showing the impact of baryonic feedback on the inner slopes (α) of dark matter halos. The slope was measured at 1.5% of the halo virial radii, using results from the NIHAO hydrodynamic simulations and from FIRE-2 collaboration simulations, and plotted against the ratio of stellar mass to the total halo mass. The shaded gray band shows the expected slopes for NFW halos with the predicted range of concentrations from dark-matter-only simulations.

As core-like density profiles have $\alpha \to 0$, we see that the core formation peaks a ratio of $M_\star/M_{halo} \approx 0.005$, which maps to stellar masses of $M_\star \simeq 10^{8-9}\ M_\odot$. At bigger ratios we see that the excess central mass can compensate and drag dark matter back in. However, at ratios below $M_\star/M_{halo} \approx 10^{-4}$, the impact of baryonic feedback is negligible. This corresponds to $M_\star \approx 10^6\ M_\odot$, and to Ultra-faint dwarfs.

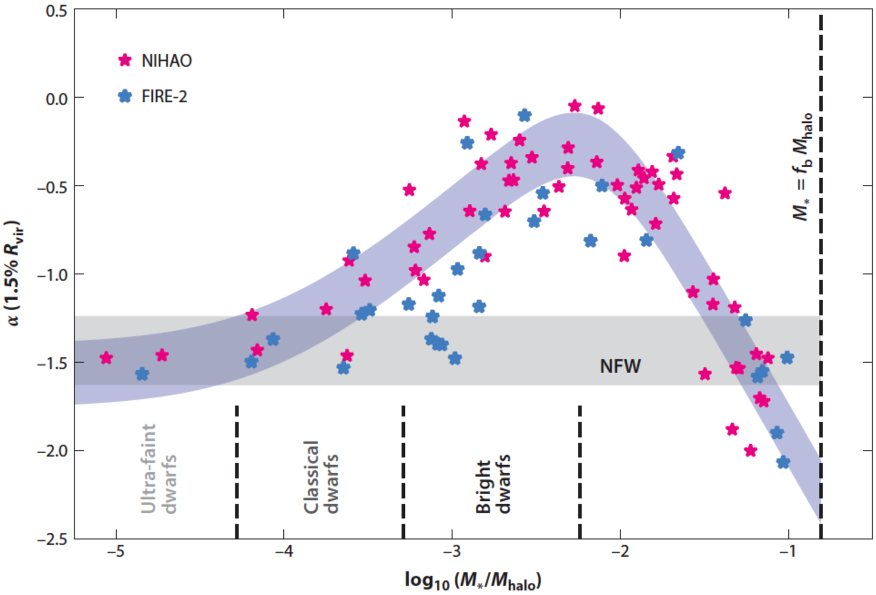

Figure 1.2: Plot of the the inner dark matter density slope (α), measured at 1.5% of the halo virial radii, as function of $M_\star/M_{halo}$ for simulated galaxies from the NIHAO cosmological hydrodynamic simulations (magenta) and from the FIRE-2 simulations (cyan). The shaded gray band shows the expected range of dark matter profile slopes for NFW profiles as derived from dark-matter-only simulations. Larger values of α imply core profiles, while values of $\alpha \lessapprox -0.8$ imply cusps.(Bullock and Boylan-Kolchin, 2017)

The effect of feedback on density profile shapes as a function of stellar mass is further illustrated in Figure 1.3 (Bullock and Boylan-Kolchin, 2017). Here, FIRE-2 collaboration simulations results are shown for three galaxies with different stellar masses, all formed in halos with $M_{halo} = 10^{10} M_\odot$. The dashed lines in each panel represent dark-matter-only versions of the same halos. It is shown, once again, that for galaxies with small stellar masses (i.e. UFDs) it is expected a more steeply slope for the inner density than what is observed for more massive dwarfs.

So, despite being a complicated task, measuring the inner density profile of UFDs is more than relevant as it potentially would corroborate (or discard) this possible solution for the *cusp-core* problem.

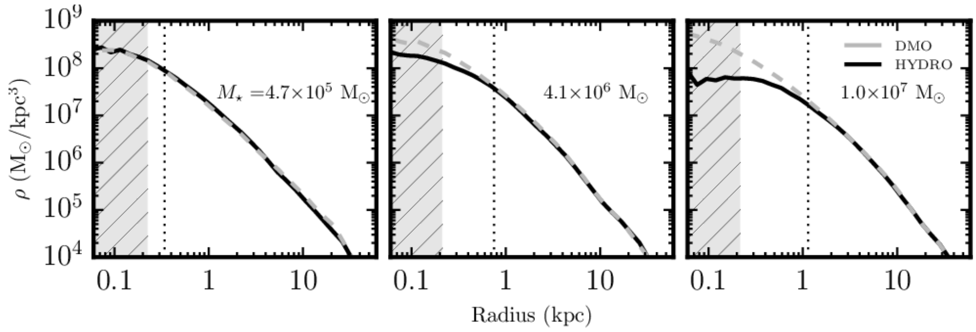

Figure 1.3: Dark matter density profiles from full hydrodynamic FIRE-2 simulations for three galaxies with different stellar masses, all formed in halos with $M_{halo} = 10^{10} M_\odot$. Solid lines show the simulations results while the dashed show the same halos run with dark matter only. The hatched band at the left of each panel marks the region where numerical relaxation may artificially modify density profiles and the vertical dotted line shows the half-light radius of the galaxy formed. (Bullock and Boylan-Kolchin, 2017)

1.4 Why Leo T?

We discussed that a large number of dwarfs were discovered in the last fifteen years, which means that many candidates are possible for a study of such system. However, due to their low luminosity, it is a difficult task to gather enough star data from a UFD in order to analyze the galaxy nature and to measure the inner density profile. Leo T presents itself as a good candidate to this project, as it is one of the brightest UFD and has already some published studies.

Leo T was discovered using SDSS imaging by Irwin et al. (2007), in Leo constellation direction. In its first observations, it was possible to estimate a galaxy distance of $\sim 420\ kpc$ and a half-light radius (Plummer radius) of $\sim 170\ pc$, from fits to the color-magnitude diagram. It was also identified a large range of stellar ages, with a young population of blue stars with age of $\sim 200\ Myr$. The intermediate-age stellar population appears to be consistent with a metallicity of $[Fe/H] = -1.6$. It was detected a compact cloud of neutral hydrogen with mass $\sim 10^5\ M_\odot$, and radial velocity of $\sim 35\ km\ s^{-1}$. The first measured absolute magnitude pointed to values of $M_V = -7.1$ (that was corrected to $M_V = -8$ in more recent studies), and a stellar mass of $M_\star \sim 10^5\ M_\odot$. All this combined makes Leo T the smallest, lowest luminosity galaxy found to date that has recent star formation and hosts neutral gas. It appears to be a transition object, hence the "T" in its name.

Even though its low luminosity, Leo T stands at the upper limit of what is considered a UFD. Despite no specific definition of such class throughout the literature, using the definition that UFDs are galaxies with $M_V > -8$ or that its stellar mass is $M_\star \approx 10^{2-5}\ M_\odot$ (Bullock and Boylan-Kolchin, 2017), makes Leo T the brightest UFD known. As a note, due to the mentioned recent star formation and presence of neutral gas, which makes Leo T unique among the UFDs, Simon (2019) suggested that only dwarf galaxies with absolute magnitudes fainter than Leo T be considered UFDs.

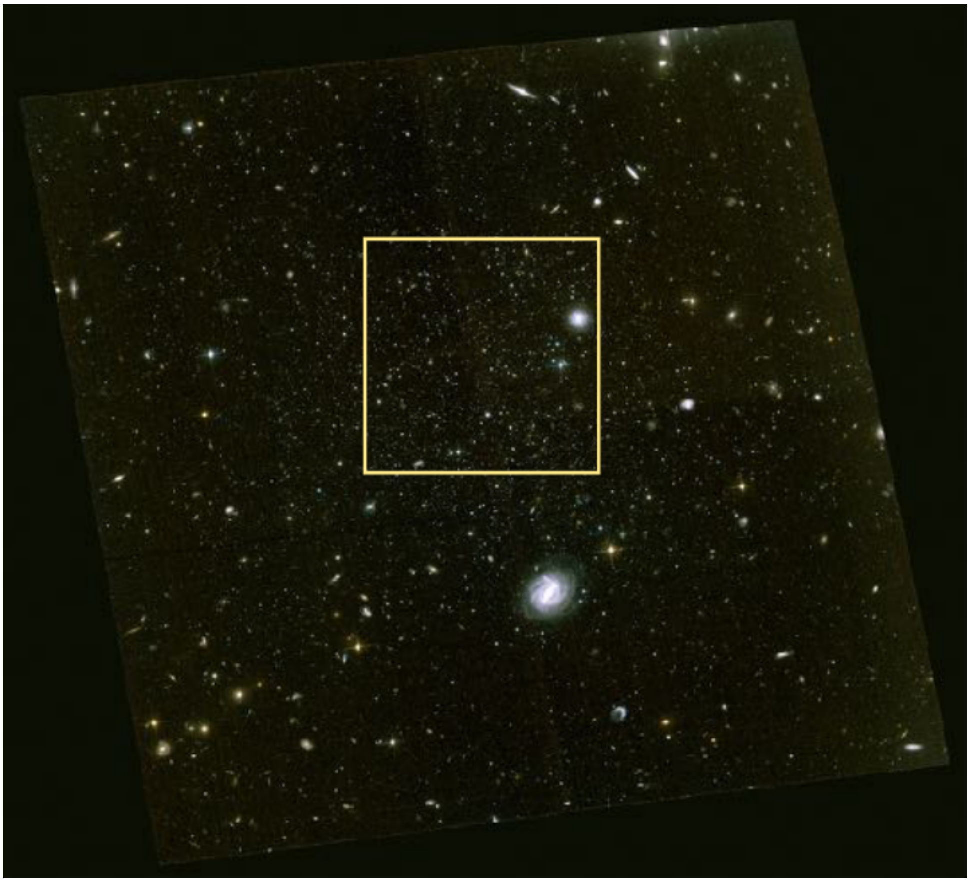

Figure 1.4: Hubble Space Telescope image of Leo T, with delimitation of the Field-of-View observed with MUSE.

1.5 Leo T Literature Review

After the discovery of Leo T, some studies, specially of photometric nature, have been carried out. In mid 2007, Simon and Geha (2007) published a Keck/DEIMOS spectroscopy study of stars of then newly discovered ultra-faint dwarf galaxies. This persists as the only spectroscopy study of Leo T until this day. In this study, 19 stars were identified as members of Leo T, measuring a radial velocity of $v_{rad} = 38.1 \pm 2\ km\ s^{-1}$ and velocity dispersion of $\sigma_{v_{rad}} = 7.5 \pm 1.6\ km\ s^{-1}$, by fitting the spectra. Similarly, it was estimated a metallicity of $[Fe/H] = -2.29 \pm 0.15$, that was later revised in Kirby et al. (2013), for values of $[Fe/H] = -1.74 \pm 0.04$. Using the equation

$$M_{total} = 167 \beta r_c \sigma^2, \tag{1.2}$$

where β is a parameter that depends on the concentration of the system, assumed to be 8, r_c is the King radii, assumed to be $r_c = 0.64 r_{Plummer}$, and σ is the observed velocity dispersion, it was calculated a total mass of $8.2 \pm 3.6 \times 10^6\ M_\odot$, corresponding to a Mass-to-Light Ratio of $138 \pm 71\ [\frac{M_\odot}{L_\odot}]$.

In the beginning of 2008, Ryan-Weber et al. (2008) presented Giant Meterwave Radio Telescope (GMRT) and Westerbork Synthesis Radio telescope (WSRT) observations, and they concluded that Leo T has both cold ($\sim 500K$) and warm ($\sim 6000K$) HI at its core with a global radial velocity of 38.6 kms^{-1}. The two components of the gas present different velocity dispersion. It was measured, for the warm neutral medium (WNM), $\sigma_v =\ 7kms^{-1}$ and for the cold neutral medium (CNM) $\sigma_v = 2\ kms^{-1}$, with a global velocity dispersion of $\sigma_v = 6.9kms^{-1}$, in agreement with the stars kinematics. Using this dispersion, it was estimated a dynamical mass of $M_{dyn} = 3.3 \times 10^6\ M_\odot$ for a radius $r = 300pc$. It was also concluded that star formation must be localized within the galaxy, associated to the presence of cold gas.

In the same year, Jong et al. (2008) presented deep, wide-field g and r photometry of Leo T, obtained with the blue arm of the Large Binocular Telescope. The data confirm the presence of both very young and much older stars, consistent with no metallicity evolution and $[Fe/H] \sim -1.5$ over the entire age of the system. There is indication of two distinct star formation bursts, with a low significance quiescent period around 3 $Gyrs$ ago. The total luminosity of Leo T is estimated to be $M_V = -8$, implying a new value for Mass-to-Light Ratio of $\sim 60\ [\frac{M_\odot}{L_{V,\odot}}]$.

In 2010, Wolf et al. (2010) derived an accurate mass estimator for dispersion-supported stellar systems, testing it with Milky Way dwarf spheroidal galaxies. By manipulating the spherical Jeans equation, they show that the mass enclosed within the half-light radius can be determined with only mild assumptions about the spatial variation of the stellar velocity dispersion anisotropy, as long as the projected velocity dispersion profile is fairly flat near the half-light radius ($r_{1/2}$), which is typically observed. Thus, they find the equation

$$M_{1/2} \simeq 3G^{-1}\sigma_{los}^2 r_{1/2} \simeq 4G^{-1}\sigma_{los}^2 R_e, \tag{1.3}$$

where σ_{los} is the line-of-sight velocity dispersion and $R_e \simeq (3/4) r_{1/2}$ is the 2D projected half-light radius. Using this equation, the kinematics results of Simon and Geha (2007) and the photometric results of Jong et al. (2008), they derived a dynamical mass of $M_{1/2} = 7.37^{+4.84}_{-2.96} \times 10^6\ M_\odot$ and a Mass-to-Light Ratio of $\Upsilon^V_{1/2} = 110^{+70}_{-40}\ [\frac{M_\odot}{L_{V,\odot}}]$.

In the beginning of 2012, Weisz et al. (2012) presented the lifetime **S**tar **F**ormation **H**istory (SFH) of Leo T based on deep imaging taken with the **H**ubble **S**pace **T**elescope (HST). It shows that 50% of the total stellar mass was formed prior to 7.6 $Gyrs$ ago. There is also evidence that Leo T star formation quenched about 25 $Myrs$ ago. Once again, it was found little evolution in the isochronal metallicities, such that over the coarse of its lifetime it is consistent with a constant value of $[M/H] \sim -1.6$. In the same year, Clementini et al. (2012) presented also a study of Leo T SFH, combined with a study of variable stars, using multi-epoch archive observations obtained with the Wide Field Planetary Camera 2 on board the HST. It was detected 14 variable stars and the distance to the galaxy was estimated to be $409^{+29}_{-27}\ kpc$. It was confirmed that Leo T has a complex star formation history, appearing to be dominated by two enhanced periods about 1.5 and 9 Gyr ago.

More recently, Adams and Oosterloo (2018) presented deep neutral hydrogen (HI) observations from the Westerbork Synthesis Radio Telescope. The mass of HI was estimated to be $4.1 \pm 0.4 \times 10^5\ M_\odot$, with almost 10% being from the CNM component. This implies that the $H1$ mass is about two times more that the estimated mass of stars of Leo T. It was estimated the velocity dispersion for each component of HI gas, with $\sigma_{CNM} = 2.5 \pm 0.1\ km\ s^{-1}$ and $\sigma_{WNM} = 7.1 \pm 0.4\ km\ s^{-1}$. The global gas velocity dispersion was estimated to be $8.3\ km\ s^{-1}$ and, using Eq. 1.3, it was estimated, for a radius of $400pc$, a dynamical mass of $M_{dyn} = 1.9 \times 10^7\ M_\odot$

In Table 1.1 is displayed a list of properties discussed above. When multiple measures are available it was selected the result of the most complete (or most recent). In the case of metallicity, as all photometric studies are in agreement with each other, it was considered $[Fe/H] \sim -1.6$.

Property	**Value**
Distance $[kpc]^{(1)}$	$409^{+29}_{-27}\ kpc$
Luminosity $[L_{\odot,V}]^{(2)}$	1.4×10^5
3D $r_{1/2}$ $[pc]^{(2)}$	152 ± 21
2D $r_{1/2}$ $[pc]^{(2)}$	115 ± 17
$v_\star$ $[km\ s^{-1}]^{(3)}$	38.1 ± 2
$\sigma_\star$ $[km\ s^{-1}]^{(3)}$	7.5 ± 1.6
$M_{1/2}$ $[M_\odot]^{(2)}$	$7.37^{+4.84}_{-2.96} \times 10^6$
$\Upsilon^V_{1/2}$ $[\frac{M_\odot}{L_{V,\odot}}]^{(2)}$	110^{+70}_{-40}
M_{HI} $[M_\odot]^{(4)}$	$4.1 \pm 0.4 \times 10^5$
v_{CNM} $[km\ s^{-1}]^{(4)}$	37.4 ± 0.1
v_{WNM} $[km\ s^{-1}]^{(4)}$	39.6 ± 0.1
σ_{CNM} $[km\ s^{-1}]^{(4)}$	2.5 ± 0.1
σ_{WNM} $[km\ s^{-1}]^{(4)}$	7.1 ± 0.4
$[Fe/H]$	~ -1.6

Table 1.1: Leo T properties gathered from the existing literature. [1]Clementini et al. (2012); [2]Wolf et al. (2010); [3]Simon and Geha (2007); [4]Adams and Oosterloo (2018).

1.6 Overview

UFDs are an amazing playground to study Dark Matter but they have a huge disadvantage. They contain so few stars that there may not be enough dynamical tracers for a robust measurement of the mass distribution. Thus, the main objective of this work is to maximize the number of Leo T stars with measured kinematics. This would allow to make a more complete study of Leo T. It should be possible to study the age and metallicity of the stars, while looking for differences in the dynamics of young and old stars and along the radii of the dwarf. Obtaining a large sample of stars with measured kinematics will also allow to derive the first ever density profile of Leo T.

Aiming for this, it was used MUSE spectrograph observations of Leo T, complemented with photometric observations. The high sensitivity of MUSE and its wide field of view should be advantages for the task proposed. Nevertheless, a thorough reduction of MUSE data is needed to be possible to gather clean spectra of stars fainter as possible. Thereby, the data used is described in Chapter 2 along with the discussion of the steps carried out for data reduction and data processing. The procedures adopted at each step and their reasons are described at Section 2.3

After that, a number of methods were used to analyze the reduced data, in order to obtain results for star kinematics, metallicity and ages, among others. These methods and their purposes are discussed in Chapter 3. The results obtained are displayed and examined in Chapter 4, while the conclusions are presented in Chapter 5.

Chapter 2.

Data of Leo T

2.1 The Multi-Unit Spectroscopic Explorer - MUSE

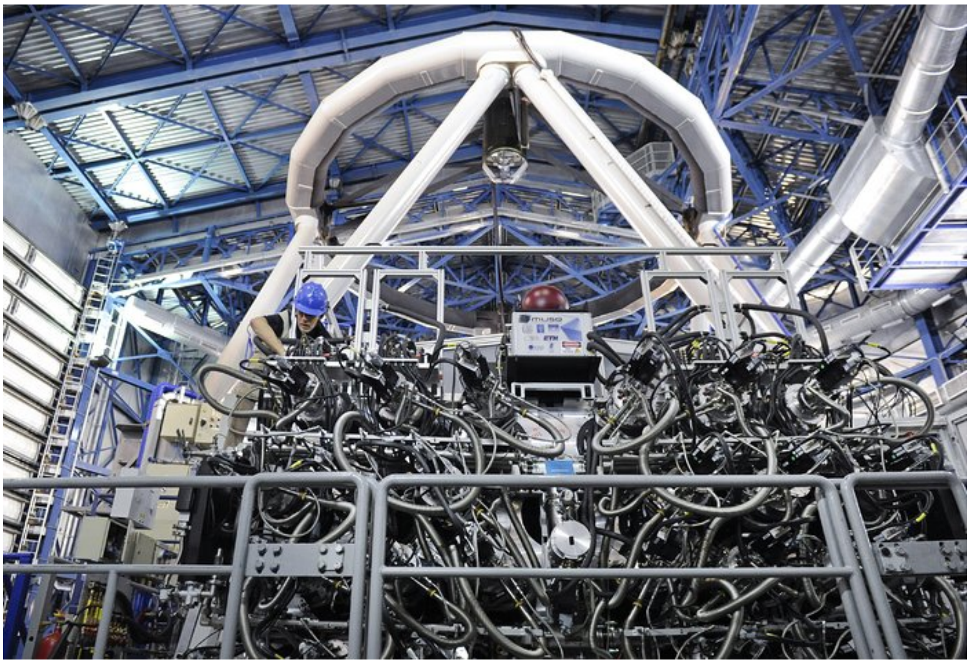

Figure 2.1: View of UT4, with MUSE on the Nasmyth B platform, in VLT, at Cerro Paranal, Chile. It has a modular structure composed of 24 individual detectors.

The **M**ulti-**U**nit **S**pectroscopic **E**xplorer, **MUSE** (Bacon et al., 2010), is a second generation instrument operating at the **E**uropean **S**outhern **O**bservatory (ESO) **V**ery **L**arge **T**elescope (VLT) **U**nit **T**eslescope 4 (UT4), and had first light in 2014. It is a panoramic **i**ntegral-**f**ield **s**pectrograph (IFS) with medium resolution, assisted by an adaptive optics system, performing in the visible wavelength range.

An integral field spectrograph is a system designed to give spectral information within a

Number of IFU modules	24
Wavelength range	480-930 nm (nominal), 465-930 nm (extended)
Detectors	24 x 4k x 4k MIT/LL CCD
AO type	noAO, Ground layer AO, and LTAO, 4x(5-10 W) lasers
Throughput WFM	14 % (480 nm) 35 % (750 nm) 14 % (930 nm)

Table 2.1: Basic technical parameters of MUSE.

two-dimensional area at every location of the **F**ield **o**f **V**iew (FoV). To achieve this, there are a spatial stage, that reformats the FoV, and a spectral stage, that disperse and focus the light on the detector. MUSE uses a two-mirrors slicer design and 24 integral-field spectrographs, or 24 **I**ntegral-**F**ield **U**nits (IFU). This design slices each image of each IFU in 48 slices. The advantage of image slicer system compared to others is data-packing efficiency.

Adaptive **o**ptics system (AO) is designed to partially remove, in real time, atmospheric distortion and, therefore, improve VLT spatial resolution. MUSE uses a system known as GALACSI, which is part of the **A**daptive **O**ptics **F**acility (AOF). As in most cases there is not bright stars in the vicinity of the desired scientific field of view, it is used four artificial stars as reference. These stars are created by a four sodium **L**aser **G**uide-**S**tars (LGS) system that excites the sodium layer on the atmosphere.

Besides **W**ide **F**ield operating **M**ode (WFM), MUSE also has a secondary operating mode, named **N**arrow **F**ield **M**ode (NFW), that has higher spatial resolution but smaller FoV, but was not used in the scope of this project. In Figure 2.1 is shown a picture of the MUSE instrument, installed at the Nasmyth B focus of Yepun (the VLT UT4 telescope). In Table 2.1 it is displayed the technical parameters of MUSE instrument, with the throughput for Wide Field Mode, as it was the one used in this project. In Table 2.2 are shown the imaging features of the data processed in next sections.

As ultra-faint dwarfs are poor in stars and the contrast against the general background is rather low, MUSE wide FoV and ability of giving spectral information about every spatial location are two main technical advantages while analyzing this type of astronomical objects. It allows to target Leo T without pre-selection of stars, which enables fainter magnitudes and to obtain spectra of closely spaced stars without worrying about fiber separations. This leads

Field of view	59.9”x 60.0”
Spatial Sampling	0.2” /pixel
Spatial resolution (FWHM)	0.3”– 0.4”
Resolving power	1770 (480 nm) – 3590 (930 nm)
Limiting magnitude (1 hr, airmass=1.0, seeing 0.8”@V)	V_{AB} = 22.64 mag (550 nm) R_{AB} = 22.70 mag (650 nm) I_{AB}= 22.28 mag (784.9 nm)
Gain in ensquared energy within one pixel with respect to seeing	2
Condition of operation with AO	70th percentile
Sky coverage with AO	70% at Galactic Pole

Table 2.2: Basic imaging parameters of MUSE Wide Field Mode with AO.

to much larger samples of stars, which is crucial to more precisely determine star abundances, metallicity distribution, velocity dispersion and radial variation. Therefore MUSE, in its Wide Field Mode, is particularly well-suited for the task proposed.

For more detailed information on MUSE see Richard, Bacon, and Vernet (2019).

2.2 Leo T Observations

The central region of Leo T was observed with MUSE as part of a GTO survey of ultra-faint dwarf galaxies, which has Jarle Brinchmann as Principal Investigator and is named MUSE-

#	Date	Exposures	Grade	AG Seeing	SGS Seeing	GL Fraction	Airmass
1	2018-02-14	3	A	0.90 – 0.97	0.52 – 0.64	0.26 – 0.61	1.34
2	2018-03-17	3	A	0.72 – 0.76	0.54 – 0.62	0.42 – 0.48	1.35 – 1.40
3	2018-04-16	1	A	0.78 – 0.82	0.66 – 0.68	0.85 – 0.88	1.34 – 1.36
4	2018-04-17	2	A	0.78 – 0.82	0.66 – 0.68	0.85 – 0.88	1.34 – 1.36
5	2019-01-06	1	D	0.97	–	0.87	1.34
6	2019-01-06	2	B -	1.01 – 1.02	0.95	0.69 – 0.76	1.37 – 1.41
7	2019-01-07	1	B	0.93	–	0.15	1.40
8	2019-04-09	3	A	0.83 – 0.98	0.47 – 0.67	0.72 – 0.78	1.34

Table 2.3: List of Leo T observations with MUSE, which totalizes 16 exposures of 15 minutes, each. It is displayed information about the Auto-Guider and Slow-Guide Star seeing, Ground Layer Fraction and Airmass (see text for more information).

Faint (Zoutendijk et al., 2020). This obervations were made between 14 of February, 2018 and 9 of April, 2019 and are referring to Run IDs 0100.D-0807, 0101.D-0300, 0102.D-0372 and 0103.D-0705.

In Table 2.3 are listed Leo T observations made for that survey, which gathered, in total, 16 exposures of 15 minutes each. The observations were scheduled to be made in groups of three exposures, which was not always possible, mainly due to technical problems. So, besides the number of exposures made in each observation, is displayed in Table 2.3 the grade of the observations, that classifies for technical conditions. There is also two estimations of the seeing, the auto-guider seeing and the slow-guide star probe seeing, where the latter is an indication of the AO-corrected seeing and estimations of the ground layer fraction and airmass.

The observations were, in general, quite successful. Nevertheless, there is a couple of problems needed to be addressed. First, the observations made in the days 6 and 7 of January 2019 were affected by technical problems, namely in LGS, which cause failures in the slow-guide star probe for observations #5 and #7, and guiding star loss for observation #5, that was graded D due to this failures. Therefore, the exposure referring to the latter was not used in the procedures described in Section 2.3, resulting in a total of 15 exposures with 3.75 hours of usable exposure time combined. Another issue detected was a bright streak caused by a satellite passing by, in the exposure corresponding to observation #3. In order to utilize this exposure, the satellite track present in the exposure was masked out, after data processing, by removing the information on the contaminated pixels in this exposure final data cube (for more information about data processing see next section).

To complement the spectroscopic data, it was also used photometric observations. It was used data from public *Hubble* Space Telescope (HST) data of Leo T, from HST Proposal 12914, Principal Investigator Tuan Do. Two images were used, referring to two different filters, both taken in 13 January, 2013. More information about this data is displayed in Table 2.4. These images, of high resolution, are useful to create a catalog of stars positions and photometric information present in the studied FoV (see subsection 2.3.9). This, besides making possible a photometric analysis of Leo T, is fundamental for the task of extracting spectra of individual stars from the spectroscopic data (see Section 2.5).

Filter	**Exp. Time** (seconds)	**Instrument**	**Apertures**	**Central Wavelength** (Angstrom)
F606W	6300	ACS	WFCENTER	5921.950
F814W	990	ACS	WFCENTER	8044.991

Table 2.4: Basic information about HST photometric data.

2.3 MUSE Data Reduction

2.3.1 Overview

As every other astronomical instrument, MUSE data needs to be carefully calibrated before being scientifically analyzed. Calibration of an instrument usually includes creation of master calibration data which is then applied to subsequent calibration steps and to the science data itself. Therefore, science observations are supplemented by on-sky calibrations done with the telescope during twilight and during the course of the night. This type of processing of raw data from modern astronomical instruments is only viable using dedicated software. Due to MUSE complexity and size of data output, a dedicated processing environment was created to be an essential part of MUSE. This is called the MUSE **D**ata **R**eduction **S**oftware, DRS, also called *the pipeline* (Weilbacher et al., 2012). In this work it was used DRS version 2.8.1 (Weilbacher et al., 2020), following the respective Data Reduction Software Manual.

In Figure 2.2 is displayed the main processing steps needed to calibrate and transform the raw data, first in a table-based intermediate format and, finally, into a data cube. So, to achieve this, the computations are split into two parts.

The first part, the so called *Basic Science Processing* (see 2.3.7), deals with calibrations and corrections of the raw science data on the basis of single CCDs, outputting individual pixel tables per IFU for each exposure. This calibrations are needed due to the nature of the instrument design, which introduces some disturbances in the raw data. Some are general to all spectographic instruments, like the bias level (2.3.3) and flat field (2.3.4) correction or wavelengths calibration (2.3.5), and others are specific for MUSE, like the need of rearranging all slices to match the FoV (2.3.6).

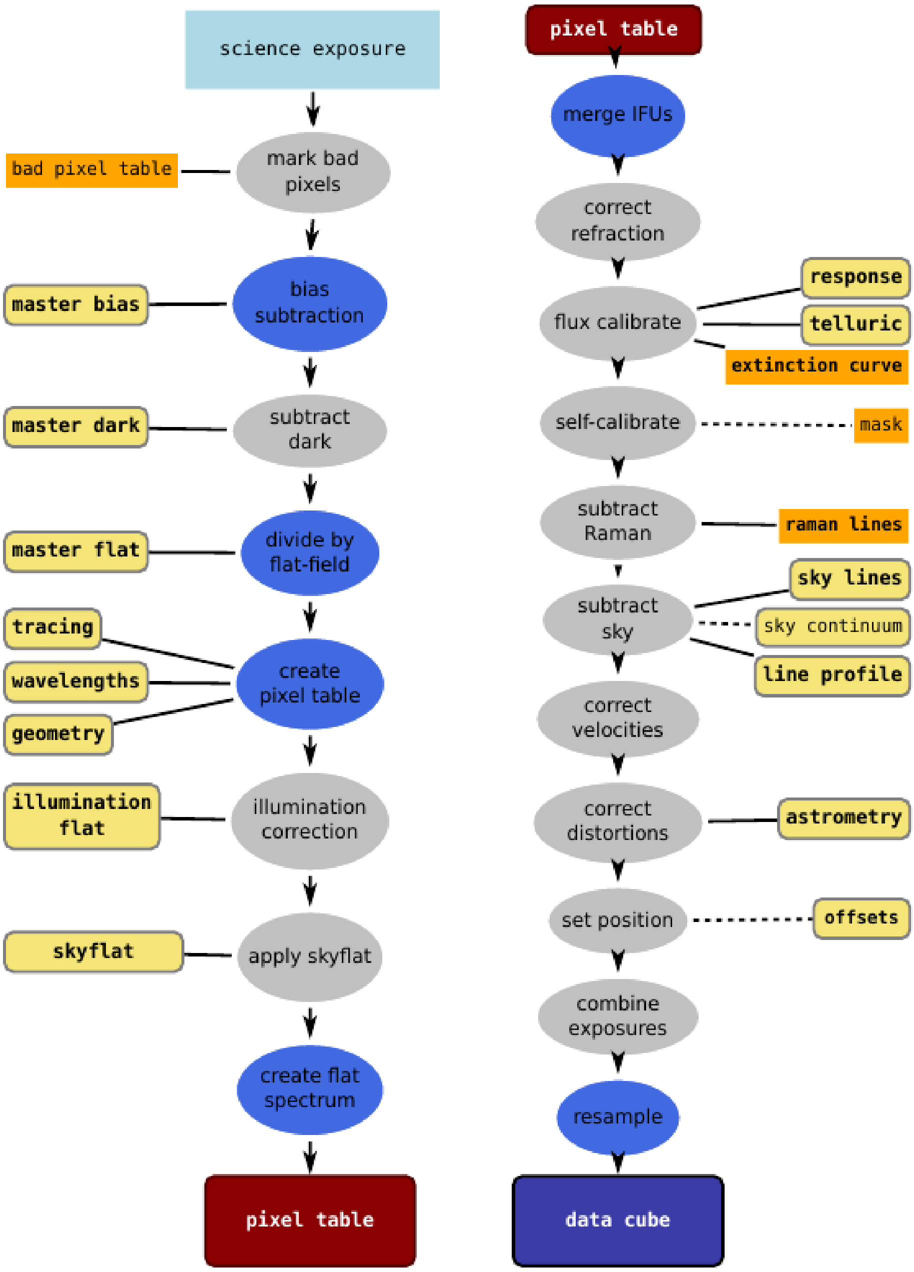

Figure 2.2: Overview of MUSE DRS steps. In the left column are shown the basic science processing steps, starting with raw science data and finishing with the intermediate pixel table. In the right are shown the science post-processing, starting with the previous mentioned pixel table and ending with the final data cube. The steps that are optional are marked in grey, while mandatory ones are in blue. The input files needed to be created have a yellow background, while the pre-existent (generic) input files have an orange background. Input files that are mandatory are connected with a solid line, dotted lines signify inputs that are not required. Source: Weilbacher et al. (2020).

This first processing part, including the calibrations and corrections, is processed in an individualized module within the pipeline, called *muse_scibasic*. This module works with the raw science exposures and computes the corrections and calibrations with the help of auxiliary calibration files. The majority of these files are created using calibration exposures that are taken during daytime with the help of the calibration unit. Different kinds of calibration exposures are used, since there are specific exposures for each type of calibration. To maximize the calibration quality, multiple calibration exposures of each kind, that are taken in sequence, are used and combined, creating a single master calibration file for each type of calibration. Furthermore, as these perturbations in the raw data can be dependent of the date of observation (or temperature), it was used calibration exposures taken very close in time to the science exposures, hence creating a set of master calibration files for each set of observations.

In the left column of Figure 2.2, which is referent to *muse_scibasic* module, are displayed, with a yellow or orange background, the calibration files needed to perform the correction or calibration mentioned in the balloon connected with a solid line. These have either a gray or a blue background: the blue background means that the calibration is mandatory, while the gray symbolizes an optional one. In the case of the different background colors of the input calibration files, the orange one concerns an input file that is inherent to the calibration, and was created by (Bacon et al., 2017). In practice, the *muse_scibasic* module will only compute the steps for which the input files are provided and will only produce a pixel table if all steps denoted with a blue background are successfully completed. Concerning this project, all steps were done, with exception of dark subtraction. Since MUSE CCDs have very low dark current (Weilbacher et al., 2020), dark calibration exposures are very time consuming and not commonly made (in fact, MUSE Calibration Plan previse only 5 dark exposures of 1800 seconds per month), allied with the fact that Leo T science exposures are not long enough to justify the effort, it was chosen to not create a *master dark* input file.

The creation of these calibration files and its purpose are discussed in the subsections between, and including, 2.3.3 and 2.3.6. This first part processing, and its main pipeline module, is discussed in subsection 2.3.7.

The second part, called *Science Post-Processing* (see 2.3.8), carries out on-sky calibrations and construction of data cubes, by merging the pixel tables created in the first part for each exposure. Then, the data cubes, or the equivalent pixel tables, of all science exposures can be combined into one final data cube. The corrections made in this part are needed to correct for contamination introduced by the conditions of observation. This calibration includes, for example, removal of sky lines or attribution of **W**orld **C**oordinate **S**ystem (WCS) coordinates. Similar to the first part, there is a module within the pipeline, called *muse_scipost*, that is responsible to process all the steps of this second part (with the exception of exposure combining). This module works with the aforementioned pixel tables and computes the corrections also with the help of calibration files. Unlike the first part, the majority of calibration exposures used in this module are not dependent on the date of observation (or temperature). So, once again, it was used calibration files created by Bacon et al. (2017), with the exception (following the right column of Figure 2.2) of response and telluric for flux calibration files and, of course, the offsets table used to set WCS positions, that were created specifically for this project, following the principles discussed above. In the right column of Figure 2.2 are displayed, with the same color scheme as before, the calibration files needed for each calibration step. This module differs from the previous in the fact that the middle steps are not mandatory and some (the ones with dashed lines or without lines at all) do not need an input file to be completed. Thus, this steps need to be activated (or deactivated) when calling the module inside the environment. In fact, the self-calibration is turned off as default (as of DRS version 2.8.1). Also, exposure combination is done in an independent module called *muse_exp_combine*. Concerning this project, all but the self-calibrate step were completed, as it was followed the default settings and recommended procedure for this module.

The purpose and creation (when applied) of the calibration files used in this part and its main module are discussed in subsection 2.3.8. The exposure combination and posterior offset correction are discussed in subsection 2.3.9.

2.3.2 Raw Data

The MUSE raw data comes in multi-extension FITS files, where each of the 24 CCD images, referring to the 24 IFU, is stored in an individual extension. Each image is 4224 × 4240 pixels in size, and stored as unsigned integers of 16 bit. The CCD is read-out on four ports corresponding to four regions of equal size, called *quadrants*. These have a data section of 2048×2056 pixels, and prescan and overscan regions of 32 pixels in width.

As an example, a raw science image corresponding to the IFU 10 of the first exposure of the first observation listed in Table 2.3 is displayed in Figure 2.3. In this image is possible to see the slices of the IFU as the vertical stripes. The blue end of the MUSE wavelength range is located at the bottom of the image, while the red limit is near the top. There is a step-pattern, which is created by the geometry of the image slicer. Are also visible the overscan regions of the CCDs, which create the cross at the image center, and the prescan regions, that originate the empty borders. This image, being a 900 second exposure, is dominated by sky emission and continuum over the zone near the blue limit, so there is a block filter that removes part of the blue light, making this zone look near empty.

Besides the 24 FITS extensions mentioned above, there are others concerned with auxiliary instruments, like the SGS system, that are not used by this *pipeline*.

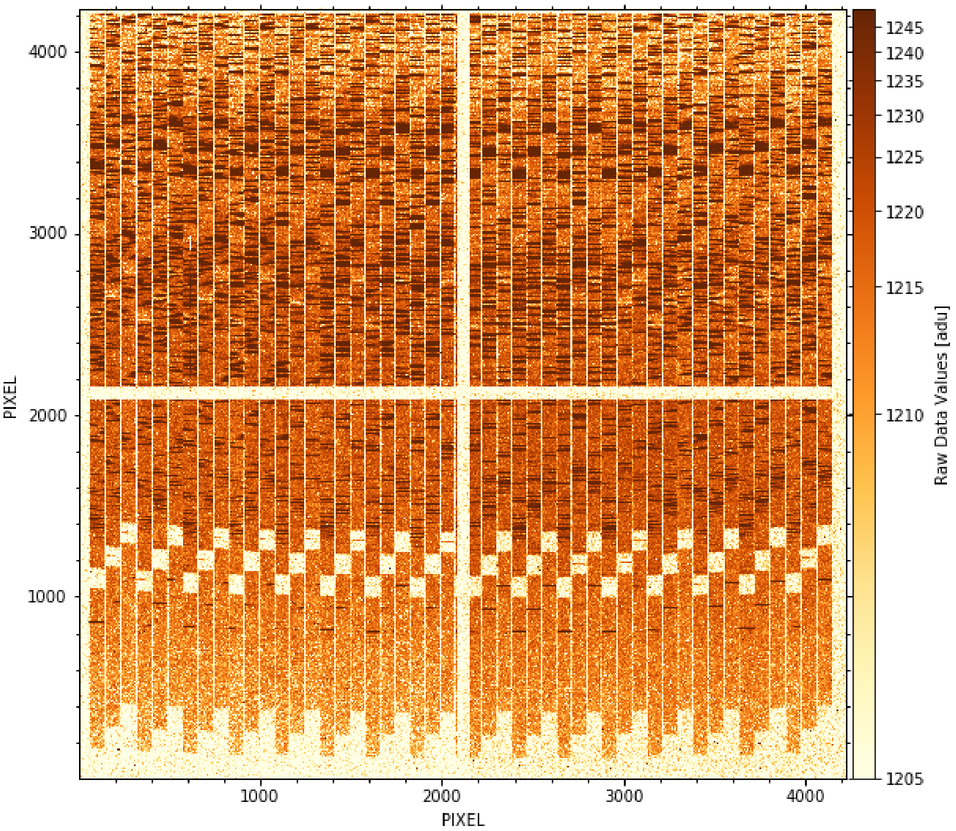

Figure 2.3: Raw science data of IFU 10 of the first exposure of observation #1 listed in Table 2.3.

2.3.3 Master Bias

The first step to remove the instrumental pattern from CCD exposures is always to subtract the bias level. The bias level is caused by a bias voltage, which is a constant offset voltage applied to the capacitor. This means that, even if no photon reaches the detector, there will still be a positive photo-electronic counting. To estimate the bias level it is usually taken a series of exposures with zero exposure time and closed shutter. Because there is no exposure time, these images contain no photo-electrons, and no thermally excited electrons. It is important to use several bias frames as, averaging all together, reduces the impact of readout noise and gives a more accurate estimate of the bias level. This combination of bias frames is called a *master bias* and can be subtracted from all science images to remove the bias level from each pixel.

In the case of MUSE, daily sequences of, typically, 11 bias frames with about one second of exposure time and closed shutter are recorded. As the CCDs are read out in four quadrants, the bias level in the middle of the read-out image exhibits four different values. On top of this, the bias frame shows horizontal and vertical gradients so that bias images have to be subtracted from science and calibration data as 2D images. In case of a variation of the bias level with time, the bias frame needs to be offset to the actual bias determined from other exposure, analyzing the overscan region. Finally, the bias images are also used to measure the **r**ead-**o**ut **n**oise (RON) of each CCD.

In MUSE DRS, the *master bias* is created using the *muse_bias* module. This recipe combines the input bias frames into one *master bias*, which contains the combined pixel values, in adu, of the raw bias exposures, with respect to the image combination method used.

In the case of this project, it was created 6 different master bias, each one combining a set of 11 bias frames recorded in a specific day. It was used the master bias created nearest in time to each one of the 15 exposures used. As the bias set is usually acquired in the morning, it was used the set taken in the morning after each science exposure.

For combining the bias frames, it was used the default values of the *muse_bias* module, except for the overscan parameter. A 3σ clipped average was used to combine each set of 11 bias frames into multiple master bias. After close inspection of the resulting master bias, it was noted that it was present some vertical lines. The overscan region is analyzed to correct for gradients that change with time, by modeling the slope of the vertical overscan with a polynomial. This polynomial is computed iteratively and its order is increased until a good match is found. As this fit was not good enough, producing the vertical lines, the polynomial order was set manually to 15.

This way, six *master bias* were created to serve as input file in the processing step described in Section 2.3.7

2.3.4 Master Flat and Trace Table

Flat-field correction is another classic step in CCD imaging processing. This correction has the purpose of correcting pixel-to-pixel sensitivity variations and to locate dark pixels. The fact that pixels in a CCD are not all exactly the same size, due to manufacturing tolerances, the possibility of dust grains on the optical surfaces, and other microscopic defects, can alter the number of counts from an object depending upon its location in the image. The common way of solving this is using *flat field* frames, that, similar to the master bias, are combined in a *master flat*.

Flat field frames are images taken using a continuum lamp, which is assumed to produce an uniform count along all the area of the CCD. Therefore, after bias subtraction (and, optionally, dark subtraction), it is expected that any variation in the flat field is due to the effects mentioned.

With respect to MUSE, daily sequences of typically 11 flat field frames with zero exposure time and with the continuum lamps switched on are taken. This flat field frames, besides serving the purpose described above, are also used to trace the position of the slices on the CCD.

In MUSE DRS, the *master flat* is created using *the muse_flat* module. This recipe combines several flat field frames into one master flat field file and traces the location of the slices on the CCD, creating a trace table. To this end, first the raw flat field images are trimmed , recording overscan statistics, and have bias subtracted. Then, the data is converted from adu to electrons using the gain and the exposures are combined into a master flat. The master flat contains the combined pixel values of the raw flat exposures, with respect to the image combination method used, normalized to the mean flux.

The trace positions of the slices on the CCD are located by finding their edges using a threshold method. This is repeated at given intervals, tracing the central position and width of each slit vertically across the CCD. A trace table is saved containing polynomials defining the location of the slices on the CCD.

The *the muse_flat* module also searches for dark or bright pixels in the image area. To speed up the process it was used a bad pixel table, created by Bacon et al. (2017).

Similar to the master bias creation, 6 master flat and trace tables were created. Exactly as for the creation of the master bias, a set of 11 daily frames was used, corresponding to the days for which the master bias were created. Each master bias was also used as input, to subtract the bias level, as well as the already mentioned bad pixel table. The default values of the *muse_bias* module were used, with exception for the overscan parameter, once more, which was change accordingly to the change made in the *muse_bias* module. Therefore, the same 3σ clipped average was used to combine each set of 11 flat field frames.

Thus, six *master flat* and *trace tables* were created to serve as input file in the processing step described in Section 2.3.7

2.3.5 Wavelength Calibration and Line Spread Function Profile

The wavelength calibration is one essential step for spectrographic data processing, as it deals with matching the data of each pixel to a corresponding wavelength. This is normally done using arc lamp exposures. These lamps produce a known spectrum, which makes possible to identify the arc lines in the arc frame and, since their wavelength is known, to make a one-to-one correspondence between pixel number and wavelength.

Five daily exposures per three different lamps are made with MUSE to this end. It is used Ne, Xe, and HgCd lamps.

In MUSE pipeline, a dedicated module, named *muse_wavecal* computes the wavelength solution for every slice on the CCD. First, the data is trimmed, the overscan statistics recorded, and bias level is subtracted. Then, the data is combined into separate images for each lamp. To compute the wavelength solution, arc lines are detected at the center of each slice and assigned wavelengths, using an input line catalog to apply pattern matching to identify lines. Gaussian centering is used to trace each line to the edges of the slice in each column of the CCD. This Gaussians also yield centering error and line properties. These analysis are done separately for different lamps, to reduce the blending amount. The final two-dimensional fit uses all positions, their wavelengths, and the given polynomial orders to compute the final wavelength solution for each slice, iteratively rejecting outliers. Because the MUSE spectrographs do not operate in vacuum, the wavelength calibration is based on arc line wavelengths in standard air.

Once again, it was created a wavelength calibration table per day of observation, totalizing 6 *muse_wavecal* outputs. It was used the set of 15 arc frames that are taken daily, combined with the input files previously created: Master Bias, Master Flat and Trace Table. The line catalog used was created by Bacon et al. (2017). Default module parameters were used, with the exception, naturally, of the overscan parameter. This solution is a two-dimensional polynomial, with a "horizontal" 2nd order polynomial describing the curvature of the arc lines in each slice on the CCD, and a "vertical" 6th order polynomial describing the dispersion relation with wavelength.

These solutions are saved in 6 files called *Wavelength Calibration Table*, and were used as input in the processing step described in Section 2.3.7 and to compute the slice and wavelength dependent Line Spread Function.

The **l**ine *s*pread *f*unction (LSF) measurement is important within the MUSE pipeline as it allows to achieve good sky subtraction and to model the laser-induced Raman lines (from the LGS system). Since the LSF is determined on data recorded by the MUSE CCDs, it implicitly includes the slit width (of the MUSE slices) and the bin width of the detector.

In MUSE DRS exists the *muse_lsf* module for this end. This module requires the same inputs as the wavelength calibration module plus the final wavelength solution derived from it. Default module parameters were used, with the usual exception. As before, the raw exposures are overscan-corrected, bias-subtracted and flat-fielded corrected. Then, the MUSE pipeline uses an interpolated 2D image, which represents the line shape as a function of wavelength, for each IFU and slice of the instrument. To do this the image of all arc exposures are converted into a special pixel table, that contains only the data around the brightest and most isolated arc lines from the line list, within a certain range from the known peak of the line. This pixel table is divided into the individual slices to fit the individual LSFs.

The computation is carried out as a 2D regression, where the x-direction is along the LSF (across the arc lines), and the y-direction is the wavelength (the central wavelength of the arc lines). For each step in LSF direction, all pixels of all arc lines within a certain distance range from the line peak are fit with a 2D polynomial of 2nd order in x-direction and 3rd order in y-direction. The LSF profile is created by evaluating all these polynomials at their nearest output image pixel and the result of all slices of each IFU are stored together, as a data cube.

This procedure create 6 LSF profiles, that were used as input in the processing step described in Section 2.3.8.

2.3.6 Twilight Skyflat Field

The MUSE calibration unit provides an illumination that very closes resembles the illumination of objects in the sky. To perfect this, and in order to remove any residual gradients, the pipeline uses bright sky background exposures called twilight skyflat frames. These exposures, which sequences start before sunset to reach high illumination levels in short exposures, resemble very well the illumination of the MUSE instrument with a constant background.

To accomplish this, 8 weekly twilight skyflat frames are created. So, and following the observations arrangement in time, 5 sets of 8 exposures were used to create 5 *twilight data cubes*, using MUSE DRS module called *muse_twilight*. Besides the mentioned skyflat frames, it was used as input for this module the previously described master bias, master flat, trace table and wavelength calibration table, chosing the ones taken closest in time to each set of twilight skyflat exposures. In addiction, it was used a *geometry table* created by Bacon et al. (2017). A geometry table is the output of a central MUSE-specific calibration called geometric calibration. This calibration has the aim of determine where within the field of view the 1152 slices of the instrument are located.

As before, default module parameters were used, with the exception of overscan fitting polynomial that was manually set to 15. As the procedure made for the other corrections, the twilight skyflats are bias-subtracted, converted from adu to electrons, flat-fielded corrected and all exposures are combined, using a 3σ-clipped average. Using the mentioned wavelength calibration, tracing solution and geometry table, each pixel in the combined images is assigned 3D coordinates (two spatial and one wavelength), creating a pixel table for each IFU. Then, the light in the wavelength region of the sodium laser light are blocked using notch filters, and pixels around this wavelength are excluded from further processing. The integrated flux in each IFU is computed as the sum of the data in the pixel table, and saved in the header, to be used as estimate for the relative throughput of each IFU. The pixel tables of all IFUs are then merged, using the integrated Fluxes as inverse scaling factors, and a cube is reconstructed from the merged dataset.

This way, the last basic processing solution was created in the form of 5 *twilight data cubes*, that were used input at the following section.

2.3.7 Basic Science Processing

The work steps discussed until now in Section 2.3 were all in preparation of the basic science processing, which is the first processing step of the actual science exposures. In MUSE DRS this is done with the *muse_scibasic* module, that takes as primary input the raw exposures of a science target. This module has the goal of removing instrumental signature from the data of each CCD and convert them from an image into a pixel table. So, in the case of this project, it was used the 15 science exposures that are listed in Table 2.3 (recall that observation #5 was discarded). As processing handles each raw input image separately, this module was computed 15 times separately. As discussed above, it was used calibration files as auxiliary input. For each science exposure were chosen calibration files that are closest in time to the aforementioned, with the exception of the *ILLUM* exposure. The ILLUM exposure is a typical flat-field with continuum lamp exposure that, unlike all other calibration exposures mentioned, is taken at night. At MUSE, these single flat fields are taken automatically at hourly intervals during the night or when the change in temperature is above 0.3 degrees. These are used to correct the relative illumination between all slices of one IFU. For each scince exposure it was used an ILLUM exposure taken in the same night and that has closest measured temperature at the time of the exposure.

Therefore, for each exposure was used, as input calibration files, a master bias, a master flat, a trace table, a wavelength calibration table, a twilight cube, an ILLUM exposure and the bad pixel and geometry tables. Default module parameters were used, with the exception due to the master bias overscan fit. First, the object raw data is trimmed, recording overscan statistics. The bias level is subtracted, the data converted from adu to electrons and divided by the flat-field. The integrated flux value from the twilight cube is propagated and the reduced image is saved a first time. The geometry table, trace table, and wavelength calibration table are used to assign 3D coordinates to each CCD-based pixel. This creates a pixel table per each IFU for each science exposure. Then, the data of each slice is multiplied by the normalized median flux of that slice in the ILLUM exposure. Finally, the data is divided by the normalized twilight cube, using the 3D coordinate of each pixel in the pixel table to interpolate the twilight correction onto the data.

This process creates 24 pixel tables per exposure, that will be combined into one pixel table per exposure using MUSE DRS module discussed in subsection 2.3.8.

2.3.8 Science Post-Processing

Science Post-processing deals with the creation of a final data cube or a pixel table for each science exposure, by merging the 24 single IFU pixel tables for each exposure. In MUSE DRS, this is done with the *muse_scipost* module. This module is also responsible for performing image calibration that is not directly related with the instrument operation. To this end, this module takes as input calibration files intended to help perform those calibrations, similar to what was done with *muse_scibasic* module. Some of those files are common to all MUSE data reductions, the so called Static Calibration Files, that were created by Bacon et al. (2017) and are listed below, with a succinct description of each one:

- Raman Lines List: After commissioning of MUSE AO system, emission lines of telluric origin were found in the spectra, that turned out to be Raman-scattered light of the laser guide stars used to stabilize the field. These appear as features originated from O_2 and N_2 and consist of bright peaks, unresolved at the spectral resolution of MUSE. Hence, this Raman lines list is used by the module to clean the Raman scattering emission lines from the data;

- Sky Lines List: List of OH transitions and other sky lines that are used to subtract the sky from the exposures;
- Atmospheric Extinction Table: File used to estimate the atmospheric extinction and help improving flux calibration;
- Filter List: List of filters that can be used to create field-of-view images;
- Astrometric Solution: Solution derived from an astrometric science frame, that is used make an astrometric calibration. This file provides a measure of the median residuals of the final WCS solution in both axes. This solution is not meant to output an absolute world coordinate system (WCS) but to give a high-precision relative coordinate solution within the spatial extent of a MUSE cube. To improve this, others solutions are used (see 2.3.9).

Besides this files, it was also used as input the LSF profile whose creation is discussed in subsection 2.3.5, that was chosen according to proximity in time with the exposures, and it was also created response curve and telluric absorption solutions using standard stars.

Standard stars are used to compute the instrument throughput and to derive a spectrum of normalized telluric absorption. The throughput is determined in the form of a response curve that is used to flux-calibrate the science data. The standard stars went through the same basic processing applied as science data. Six standard exposures, corresponding to the six main days of observations, were used to this end. They were put through the procedures of *muse_scibasic* module, using, as calibration files, a master bias, a master flat, a trace table and a wavelength calibration table, using the ones closest in time with each exposure. It was used also the geometry table mentioned above. It was used default module parameters, with the usual exception. This process, of course, created 24 pixel tables for each exposure. Then, in order to createthe two solution, it was used an dedicated module called *muse_standard*. This module runs each set of 24 pixel tables individually, and it was used, as auxiliary input, the already mentioned atmospheric extinction table and a flux reference table for standard stars. The latter is used to compare measured fluxes to tabulated fluxes in order to derive the sensitivity over wavelength.

Default module parameters were used, hence the pixel tables from all IFUs are merged and correct for differential atmospheric refraction. To flux response curve is derived by integrating the flux of all objects detected within the field of view. After deriving the sensitivity over wavelength, the sensivity curve is used to mark wavelength ranges affected by telluric absorption. Then, an interpolation over the telluric regions is made and it is derived a telluric correction spectrum for them. The final response curve is then linearly extrapolated to the largest possible MUSE wavelength range and smoothed. This creates six response curve and telluric absorption solutions that are used as input in the *muse_scipost* processing, according to the day of the exposure that is being processed.

The *muse_scipost* module, using all the auxiliar inputs mentioned above, ran individually on all 15 exposures. Default module parameters were used, with no exceptions. First the pixel tables from all IFUs are merged, for each exposure. Then, they are corrected for differential atmospheric refraction and for telluric absorption. A flux calibrated is carried out using the given response curve. Next, the slice autocalibration is computed and the flux correction factors are applied to each merged pixel table. The Raman scattering emission lines are cleaned from the data and the sky subtraction is carried out. Afterwards, the data is corrected for the radial velocity of the observer (barycenter) and the astrometric solution is applied. At this point each esposure is fully reduced and a pixel table and a data cube are saved for each exposure. It was chosen to create four FoV images for each exposure, by selecting the filters to be used from the input filter list, in order to detect some abnormality that could be present in the FoV. It was created a white-light image, and three images corresponding to the filters Johnson V, Cousins R and Cousins I. The next step consists in combining all 15 exposures into one final data cube.

2.3.9 Final Data Cube

To create a single data cube, all the exposures are combined using *muse_exp_combine* module. This module uses the pixel tables created for each exposure and combines them in one single

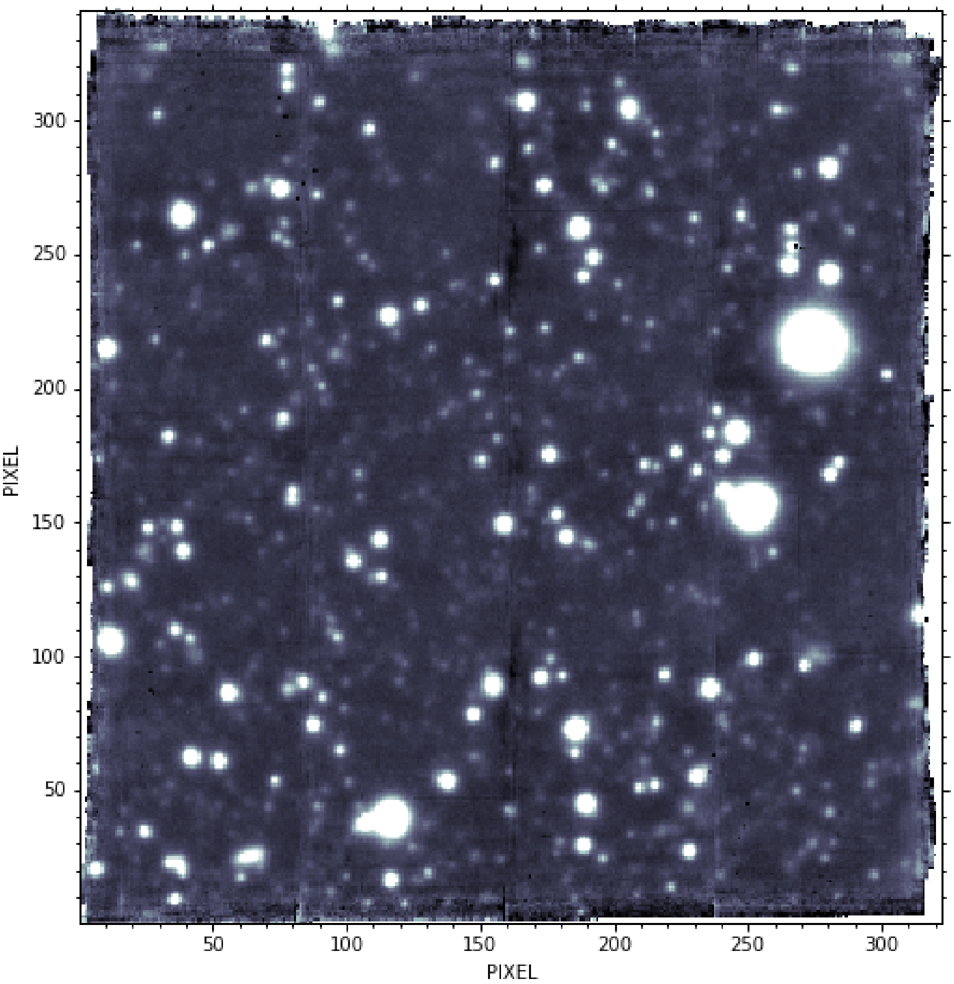

Figure 2.4: White-light image of the final data cube, with the axis indicate the size in pixel of the spatial dimensions of the datacube. This image was created by integrating each spatial pixel in all wavelengths.

data cube. This is done in a straightforward way. First, the input pixels are sorted into three-dimensional grid cells, each representing one output voxel (a 3D pixel). Each grid cell can contain no pixel or many pixels, and the pixels are assigned to the cells in a nearest neighbor fashion, depending on their 3D coordinates with respect to the coordinates of the grid cells. As multiple pixel tables enter the process, multiple pixels may be assigned to each grid cell, where exposures overlap. To compute the data value of the output voxel, each input pixel is assigned a weight that depends on the re-sampling method chosen. As default settings were used, a drizzle-like re-sampling (Weilbacher et al., 2020) was carried out to construct the combined data cube. In this case, the weight for each pixel is computed using the geometrical overlap between pixel and voxel. The calibrations applied to the data ensure that the coordinates of the center of each pixel within the output grid are known to high accuracy. As the exposures could not be perfectly aligned it was used as an auxiliary input to this module an offset list. This list was created with *muse_exp_align* module, that takes as input a white-light image for each one of the exposures. This module computes the coordinate offset for each input FoV image with respect to a reference. The source positions used to compute the offsets are obtained by detecting point sources in each of the input images.

The final data cube has 322×341 pixels, referring to two spatial dimensions, and 3722 spaxels, referring to the spectral dimension. In , this corresponds to 3722 frames of 322 × 341 pixels, with each frame corresponding to an individual wavelength.

After a first analysis residual sky signatures were detected. In order to improve this, ZAP was ran on the data cube. The **Z**urich **A**tmosphere **P**urge (ZAP) is a high precision sky subtraction tool which can be used as an enhancement to previously sky-subtracted MUSE integral field spectroscopic data. The method uses an approach based on principal component analysis to isolate the residual sky subtraction features and remove them from the observed data cube.

In Figure 2.4 is displayed a white-light image of the final data cube. Three vertical lines are still visible, corresponding to the division of the four quadrants of the CCDs. The trimming of the overscan is also not very clean, as expected.

2.3.10 Alternative Data Cube

For a parallel project, that aimed to search for Dark matter in the form of **A**xion-**L**ike **P**articles (ALPs) by exploiting their coupling to photons, it was created a secondary data cube.

Starting with the 15 individual exposures data cubes created following Section 2.3.8, it was re-estimated the pixel-to-pixel variance directly from each datacube, using the method described in Bacon et al. (2017). This was done to address the known issue that the MUSE DRS underestimates the uncertainties in the final data cube since the covariance terms are neglected. To do that, first the bright sources on each datacube were masked. To create a mask, it was used a segmentation image output by SExtractor (Bertin and Arnouts, 1996) using the photometric data from HST (see Section 2.4). Then, the **M**edian **A**bsolute **D**eviation (MAD) was estimated in each wavelength. As MAD is related to the standard deviation through a scale factor that depends on the distribution, it multiplied it by the normal distribution scalar factor. The resulting standard deviation was multiplied by the correction factor to account for the correlations, as described in Bacon et al. (2017). Finally, the one-exposure datacubes were combined using MPDAF (Piqueras et al., 2017) and the calculated variance for each pixel. The data cube thus created has the same dimensions of the data cube of Section 2.3.9. Note that for this data cube it was chosen not to use ZAP for sky subtraction.

The analysis of this data cube allowed to obtain the results discussed in a paper by Regis et al. (2020). Their results are discussed in Section 4.4.

2.4 Photometric Source Catalog

In order to better analyze the data cube, a list of sources was created using the photometric data mentioned in Table 2.4 and using SExtractor (Bertin and Arnouts, 1996). SExtractor is a program that builds a catalog of objects from an astronomical image. It uses a thresholding technique to detect sources followed by a deblending routine to separate neighbours that have been extracted as a single source. It also estimates isophotal and circular aperture magnitudes, and uses them to give the best estimate of the total magnitude for an object. This software was applied on both HST images. First it was used the F606W filter image, to create the first source catalog. Then the pixel grid created was reused to measure object characteristics exactly at the same positions and through the same apertures for the F814W filter image. This allowed the derivation of more precise color indices.

Besides the photometric data, this catalog is fundamental to help guiding the spectra extracting software to find relevant sources. After comparing the catalog with the data cube, it was found an WCS coordinates offset between HST FoV and the final data cube FoV. To correct for this, a manual analyses of the data cube FoV was carried out, comparing the position of several sources with the HST positions and estimating the differences between both. Then the mean of these differences was taken and corrected in the offset list described in 2.3.9. Then, the module *muse_exp_combine* was ran once more, as described in 2.3.9, in order to align the data cube WCS coordinates with the HST images.

2.5 PampelMuse - Extracting Spectra

The last step in data processing is to extract spectra from the sources present in the data cube. To do this, there is the need to selecting accurately the pixels corresponding to each source in the FoV in order to measure the corresponding fluxes as accurately as possible. However, this comes as a challenge, as the FoV is densely populated and the angular resolution is not very high, in the case of the data that we are dealing with. So, in each one of the data cube images, each source is represented by the **p**oint **s**pread **f**unction (PSF) characteristic of the system, scaled and shifted according to brightness and position of the source in the FoV, respectively. Thus, various PSFs can be overlapping and have to be disentangle.

In order to overcome this challenge it was used a software package, that has the purpose of facilitating the analysis of integral-field spectroscopic observations of crowded stellar fields, called *PampelMuse* (Kamann, Wisotzki, and Roth, 2012). This software uses an high-fidelity input source catalog (e.g. from HST data) to identify and locate sources in the data cube. Then, it performs a global fitting of the PSF, which is wavelength dependent, by simultaneous fitting the full ensemble using a Moffat profile. Finally, it measures the flux of each source at all wavelengths, thus creating a spectrum for each source. This package provides several subroutines to perform the individual steps described above, and their use are described in the following subsections.

2.5.1 Selecting Sources

The first step in this analysis is to identify the sources in the data cube FoV. As PampelMuse does not perform sophisticated source detection in the data cube, a subset of the source catalog mentioned in 2.4 was used as input. As HST has higher spatial resolution than MUSE and, in this case, it can resolve sources with higher magnitude (it was estimated that, for the total MUSE exposure time used, the limiting apparent magnitude is ≈ 25), the source catalog includes much more sources than the ones resolved in the data cube. So, this subset includes all sources with apparent magnitude < 25.5 (in F606W filter), in order to facilitate the identification of sources in the data cube. The input source catalog contains information about the position of the selected sources in WCS coordinates and the value of the apparent magnitude estimated using the F606W filter image. The identification of sources for which it is feasible to extract spectra from the data cube is done with the *INITFIT* subroutine.

This routine, first, creates an image from the IFS data and a mock image from the sources in the reference catalog, both in the passband of F606W filter. The mock image is prepared using the same pixel-size as the data cube and using an initial guess of the PSF (it was used default parameters). Then, a cross correlation of the two images is carried out, in order to find the most likely location of the data cube field of view with respect to the reference catalog. Because the WCS offset between the IFS data and the HST data was corrected manually, this subroutine was used in interactive mode. This mode allows to check the cross correlation and make adjustments to it by using a graphical user interface. After making small adjustments, a **s**ignal-**to**-**n**oise ratio (SNR) estimation for all sources is carried out. Then, it is made the actual source selection by looping over all sources and selecting the ones that comply with various parameters. Thus, only the sources that have $SNR > 1$ and that have no brighter source in the direct vicinity. The SNR cut also deals with the sources that are outside the IFS field of view, while looking for brighter sources in the vicinity of the sources deals with the resolution limit, to determine if the source is considered resolvable to a brighter one or not. Then, to account for the spectrum of the night sky, one or more non-stellar components are included in the fit to account for background sources. All sources that fulfill the criteria discussed above are saved in a multi-extension FITS-file, hereafter called PRM-file, that is loaded by all other routines of PampelMuse.

2.5.2 Extracting spectra

The PampelMuse routine that actually performs the extraction of the spectra by simultaneously fitting a PSF to all sources that have been identified as resolvable is called *CUBEFIT*. This routine was used following the recommended analysis strategy, in the PampleMuse manual. Thus, a first extraction with CUBEFIT is made, setting a binning of 50 in the spectral direction, in order to optimize the PSF parameters and the coordinate transformation across the whole wavelength.

This routine starts by analyzing the data cube frame by frame, starting from the central layer and simultaneously proceeding into the red and the blue part of the cube, and performing an interative analysis in order to extract the optimal flux for each source identified in the PRM-file. This analysis can be summarized as follows. A first fit of the fluxes is made, using the initial guesses of the PSF and coordinates transformation. Then, an update of the coordinate transformation from reference to IFS coordinates is made and it is performed an optimization of the PSF parameters, using the fluxes and the updated coordinate transformation. After that, the updated PSF and coordinate transformation are used to refit the fluxes of the sources, while checking if the fluxes converged. If the convergence criterion is not fulfilled, the iteration continues with fitting the coordinate transformation parameters once again. Otherwise, if the convergence criterion is fulfilled or the maximum number of iterations (10 as default) has been reached, the analysis is continued with the next layer. After all layers have been analyzed the results are written to the PRM-file.

Subsequently, a routine called *POLYFIT*. This serves two purposes: It allows a visual inspection of fitted parameters, and can be used to fit wavelength dependencies of the PSF parameters and the IFS coordinates with polynomials. This routine was used due to the latter purpose. The idea behind this is that, because of the limited SNR in each layer, the fitted variation with wavelength will show scatter, especially in spectral regions were the signal is low like telluric absorption bands. Fitting those variations with polynomials averages out the scatter, which leads to a higher SNR in the extracted spectra. It was used a normal polynomial of 3rd order. The results are, once again, written to the PRM-file.

Then, CUBEFIT was used again, this time without any spectral binning, in order to refit the fluxes, using the polynomial fits to the positions and PSF parameters. Finally, all the extracted spectra is stored in individual FITS files using the routine *GETSPECTRA*. This created 271 stellar spectra files and 1 due to a sky component.

The quality of this extraction was analyzed in different ways. First a routine called *SUBTRES* was used. This routine outputs a white-light image of the data cube FoV were all extracted sources were subtracted. This indicates if any source or any residue was left behind in the

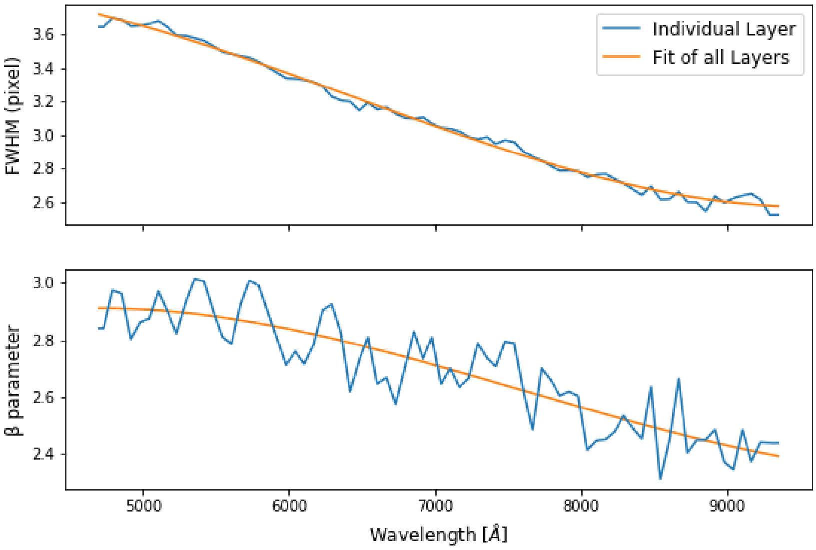

Figure 2.5: Plot of the variation of FWHM and β with wavelength (see main text).

extraction. The result was pretty clean, meaning that the source localization and extraction was successful. Then, the dependence of recovered PSF parameters in wavelength was analyzed. Two parameters are by PampelMuse to characterize the Moffat profile of the PSF. The first one is the **f**ull **w**idth at **h**alf **m**aximum (FWHM), which measures the profile width and is measured in units of pixels. The second shape parameter is β, which measures the kurtosis of the profile. Higher values of β correspond to less pronounced profile wings. A plot of the variation of this two parameters with wavelength is displayed in Figure 2.5. In this plot is displayed in blue the values estimated per each layer, while a fit for all values is displayed in yellow. It is visible that the PSF width is better constrained than the β parameter. This was expected, due to the fact that β governs the outer wings of the PSF, where the signal is generally low. This also implies that errors in β do not influence the overall optimization as much as mismatches in FWHM. We can also see that the FWHM decreases with wavelength, meaning that the red part of the cube has more resolving power than the blue part. This is a good indication as it corroborates the indication of the MUSE technical information. The final inspection of the spectra was made manually, by checking each spectrum individually, using *MARZ* (Hinton et al., 2016). This led to the identification of 19 galaxies spectra, usually late type emission galaxies. It was also identified three emission lines stars, which are discussed in Section 4.1.3. Even though the majority of the spectra contained some noise, it was detectable absorption lines characteristic of stars in almost all of them.

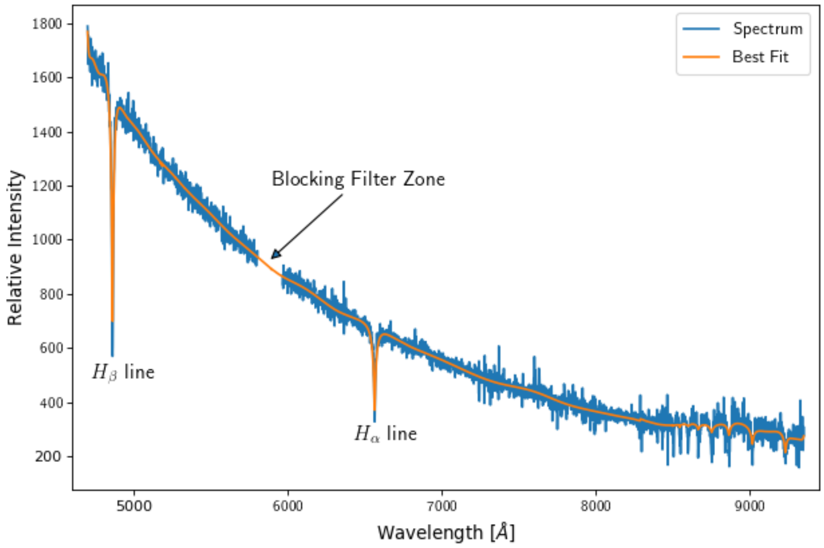

Figure 2.6: Example of a spectrum extracted with PampelMuse. It is identified the two most distinctive absorption lines and the zone filtered in order to remove the light from the laser-guide star system (see main text).

An example of a stellar spectra is displayed in Figure 2.6. This star spectrum, which is one with the highest SNR, is from a hot blue star and has very distinctive absorption lines of $H\alpha$ and $H\beta$, that are identified in the image as such. It is also identified in the image the filtered zone due to remove the light from the laser-guide star system, in the zone of sodium absorption. In yellow is plotted the best fit made in the analysis described in Section 3.1.

Hence, after extracting the spectra for each source present in the data cube FoV, the data reduction is completed and the data are ready to be analyzed.

Chapter 3.

Methods for Data Analysis

3.1 Spectroscopic Analysis

3.1.1 Fitting Spectra

After completing the reduction of the IFS data, we are left with individual spectrum files for each one of the sources identified in the data cube FoV. As discussed before, the spectra was analyzed manually an 19 spectra of galaxies were identified and, therefore, not used in this analyses. The 252 star spectra used contain many singular characteristics that allows to infer some stellar properties, if those characteristics are well known or already observed in other stars. Thus, in principle, by comparing the extracted spectra with well known spectra it is possible to estimate abundances, effective temperature, surface gravity, and metallicity of the stars.

In order to achieve that, it is possible to use stellar spectral libraries. This libraries can be empirical, i.e. observed spectra from well studied stars that serve as reference, or synthetic, i.e. construct spectra using the current knowledge of stellar evolution and nuclear physics. The use of empirical libraries has the advantage of guaranteeing real physical spectra. This improves the possible match with other observations, as absorption lines created by atomic and molecular transitions should appear at the same exact position, with the same shapes and strengths. However, these libraries are, usually, limited in spectral resolution and wavelength coverage. To assemble an extent library, a lot of effort and observing time is needed, which is very impractical. Furthermore, as the stars used in the library are studied using the same principle, the stellar properties are not known exactly, resulting in possible systematic errors.

On the other hand, synthetic libraries are limited by the completeness of the spectral line lists and by the knowledge of line broadening parameters and numerical assumptions. Apart from that, these libraries have many advantages, as the range of stellar parameters, elemental abundances, and both the wavelength range and the spectral resolution can be adjusted as needed.

The primary library used in his analysis was an synthetic library and is commonly known as *PHOENIX grid* (Husser et al., 2013). This is a library of high-resolution synthetic spectra based on the stellar atmosphere code PHOENIX. (Husser et al., 2013) used that code to create model atmospheres and to derive detailed synthetic stellar spectra from them. This synthetic spectra cover the wavelength range from 500 to 55000 $\mathring{A}$ with resolutions of $R = 500000$ in the optical and near IR. The parameter space covers temperatures of $2300K \leq T_{eff} \leq 12000K$, surface gravity $0.0 \leq logg \leq +6.0$ [cgs units], the abundances of the α elements (O, Ne, Mg, Si, S, Ar, Ca, and Ti) $-0.2 \leq [\alpha/Fe] \leq +1.2$ and overall metallicity $-4.0 \leq [Fe/H] \leq +1.0$.

When trying to fit an observed spectrum against a grid of synthetic ones, the easiest way is to correlate it with every single spectrum in the grid and find the one that matches best. However, in order to refine accuracy, a more practicable approach is to interpolate spectra for every set of parameters that does not exist in the grid. In order to do this it was used a software called *spexxy* (Husser, 2012).

This tool performs a full-spectrum fit to the observed spectrum, using interpolation over a grid of PHOENIX model spectra, as mentioned above. It was used version 2.5 of the software package, that contains many tools. It was used the *spexxyFitParams*, which determines simultaneously all atmospheric parameters and the line-of-sight velocities (v_{rad}) using a weighted non-linear least squares minimization against PHOENIX spectra. The velocities are measured using Doppler's law and line broadening. Therefore, the fit can be done with six free parameters: the effective temperature T_{eff}, the logarithm of the surface gravity $logg$, the global metallicity $[Fe/H]$, abundances of the α elements $[\alpha/Fe]$, v_{rad} and line broadening σ. When running this tool, it was chosen a linear interpolated, and the σ and $[\alpha/Fe]$ parameters were not fitted, and were fixed. The latter was fixed as the quality of the spectra is not high enough to distinguish between different values of this parameter, while the first was by indication of the tool authors.

This leave four free parameters to be fitted. After the fitting, spexxy outputs a table containing the fitted values for the four parameters and its estimated errors. It also gives information about the convergence of the fitting. So, if a fit does not converge it is not successful and the result cannot be utilized in further analysis. This unsuccessful results occur, usually, in very noisy data. The three emission lines stars were, also, not successfully fitted, as this type of stars are uncommon and are not covered by the library used. From the 252 initial spectra, 130 were successfully fitted.

As a independent check to the validity of this results, and following the approach of Roth, Martin M. et al. (2018), it was used the *ULySS* code and the empirical *MIUSCAT* library as an alternative to fit the spectra[1]. Using this, the fit can be done in two ways. The first way is to select the most approximate spectrum in the library and use it to fit the v_{rad}, adopting all atmospheric parameters of the selected reference. The second method is to fit multiple reference spectra to different wavelengths of the observed spectrum, using a multiple fitting to estimate v_{rad}. As this software needs inspection of the results while fitting, it was only fitted the spectra selected as members of Leo T (see Section 4.1.1), including the three emission lines stars.

3.1.2 Velocity and Metallicity distributions

After fitting the spectra, many stellar parameters are estimated for each star. Among these parameters, the radial velocity stands out. The velocity of Leo T stars should follow the same distribution, as its radial velocity is mainly caused by the gravity of the galaxy. In this sense, it is possible to estimate the mass of Leo T and put constraints on its dark matter by using the velocity distribution dispersion. In a similar way, as it is expected that this galaxy has had little or no evolution since its formation, the metallicity of the stars should have small dispersion.

In order to estimate the intrinsic mean value and dispersion for Leo T velocity and metallicity, it is possible to use a **M**arkov-**c**hain **M**onte-**C**arlo (MCMC) approach. To this end, it was used the code created by Zoutendijk et al. (2020).

It is assumed that the velocity and metallicity distributions of Leo T members follow a

---

[1] This second fit of Leo T stars spectra was made by Martin M. Roth.

gaussian distribution. Hence, assuming that each star has a likelihood of belonging to the Leo T that is given by m_i, the global likelihood is given by

$$\mathcal{L}(\mu_{int}, \sigma_{int}|x_i, \epsilon_i) = \prod_i \left[m_i \frac{1}{\sqrt{2\pi}\sigma_{obs,i}} \exp\left(-\frac{1}{2} \left(\frac{x_i - \mu_{int}}{\sigma_{obs,i}} \right)^2 \right) + (1 - m_i)U(v_i) \right], \qquad (3.1)$$

where μ_{int} and σ_{int} are the intrinsic mean value and intrinsic dispersion of both Leo T parameters in study. The value $\sigma_{obs,i} = (\sigma_{int}^2 + \epsilon_i^2)^{1/2}$ is the observed velocity/metallicity dispersion for each star i, while x_i denotes the measurement and ϵ_i the measurement uncertatinty of the parameter for each star. The likelihoods were calculated on a linearly spaced grid, using the limits of $\mu_{int} = 20 - 70 kms^{-1}$ and $\sigma_{int} = 0 - 30 kms^{-1}$ for the velocity, and $\mu_{int} = -2.5 - 0$ and $\sigma_{int} = 0 - 1$ for the metallicity. Using uniform priors, it was multiplied the calculated grids of likelihoods for each scenario with the respective prior factor and marginalized over the membership scenarios. It was used emcee (Foreman-Mackey et al., 2013) to constrain the parameter space. To display the final results, it was used the *PYTHON* package *corner.py* (Foreman-Mackey, 2016).

The results of the fits using the method mentioned above and the posteriors of the MCMC analysis are discussed in Chapter 4. The resulting *corner* plots are displayed in A.

3.2 Photometric Analysis

In order to take advantage of the photometric data and perform a photometric analysis, it was used PARSEC stellar tracks and isochrones (Bressan et al., 2012) to plot a color-magnitude diagram.

To generate the stellar isochrones, the online CMD 3.3 input form was used, maintaining the main default settings. Thus, version 1.2S of the PARSEC tracks was used, selecting the HST/ACS WFC photometric system, to match the system used in the photometric images mentioned in Table 2.4. It was set an interstellar extinction of $A_V = 0.1$ magnitudes, which was aplied using extinction coefficients computed star-by-star. The value of the extinction was chosen to best fit the photometric data of Leo T. For the initial mass function it was used the

Kroupa (2001), which is corrected for unresolved binaries. Finally, it was fixed a value of -1.6 for metallicity.

In order to cover a wider age range, three different isochrone tables were created, corresponding to different ages. For the first table it was defined ages from 10^8 to 10^9 years, with a step of 3×10^8 years. The second table has a fixed age of 1.5×10^9 years, while for the final table was set ages from 5×10^9 to 1.1×10^{10} years, with a step of 10^9 years.

These generated three isochrone tables, from which data corresponding to filters $F606W$ and $F814W$ was extracted. The values were corrected for the distance to Leo T, and the magnitude of filter $F814W$ was plotted as function of the difference $F606W - F814W$. Leo T photometric data was plotted, in a similar manner, against this results, which is shown in Figure 4.2.

3.3 pyGravSphere - Obtaining density profiles

There are a few methods developed in order to determine the density profile of DM dominated systems. A commonly used method is GravSphere (Read and Steger, 2017), which is a non-parametric higher-order Jeans analysis method. This method, assuming spherical symmetry, directly calculates the dispersion of the measured line-of-sight velocities in bins at different radii and two higher-order moments in the radial bins, known as the virial shape parameters.

In this project, it was used pyGravSphere, a $PYTHON$ implementation of the GravSphere method by Genina et al. (2020). This software takes, as input, a table containing only the measured star kinematics and their distance to the galaxy center. pyGravSphere has a number of models built in, in order to model the density profile, the light profile and the velocity anisotropy. To perform the analysis it was used the procedure described in Genina et al. (2020). Thus, to model the velocity anisotropy it was used the Baes and Van Hese (2007) model,

$$\beta(r) = \beta_0 + (B_\infty - \beta_0)\left(\frac{1}{1 + (r_0/r)^\eta}\right), \tag{3.2}$$

where β_0 is the central value of the anisotropy, β_∞ is the value at infinity, r_0 is the radius of transition and η is its steepness.

The tracer profile was modeled with the sum of three Plummer (1911) components ($N_P = 3$),

$$\nu(r) = \sum_{j}^{N_P} \frac{3M_j}{4\pi a_j^3} \left(1 + \frac{r^2}{a_j^2}\right)^{-5/2}, \tag{3.3}$$

with masses M_j and radii a_j.

pyGravSphere has two density profile models built-in, and both of them were used. The first one is a split power-law model with 5 spatial bins defined as spaced fractions of the half-light radius R_e, with bins $r_j = [0.25, 0.5, 1, 2, 4]R_e$. Within each bin, the density follows a power-law, being the overall distribution described by

$$\rho_{PL} = \begin{cases} \rho_0 \left(\frac{r}{r_0}\right)^{-\gamma_0}, & \text{for } r < r_0 \\ \rho_0 \left(\frac{r}{r_{j+1}}\right)^{-\gamma_{j+1}} \prod_{n=0}^{n<j+1} \left(\frac{r_{n+1}}{r_n}\right)^{-\gamma_{n+1}}, & \text{for } r_j < r < r_{j+1}, \end{cases} \tag{3.4}$$

where rho_0 is the density at r_0 and γ_j represent the slope of each power law.

The second model available is the profile proposed by Zhao (1996),

$$\rho_{zhao}(r) = \frac{\rho_0}{(r/r_s)^{\gamma}(1 + (r/r_s)^{\alpha})^{(\beta-\gamma)/\alpha}}, \tag{3.5}$$

where $r|s$ and ρ_0 are the scale radius and scale density, γ is the inner slope, β the outer slope and α governs the steepness of transition between γ and β.

As a special case of this profile, it is possible to set $(\alpha, \beta, \gamma) = (1, 3, 1)$ to obtain the NFW profile (1.1) discussed in Section 1.3.

pyGravSphere uses emcee (Foreman-Mackey et al., 2013) to constrain the parameter space. Due to the limited quantity of data and the degeneracy between some of the parameters, some of the default pyGravSphere priors on the parameters were changed. The minimum value of r_s was set to, roughly, the distance of the inner star to the centre of Leo T, as there is not a probe for smaller scales.

The maximum central density was adjusted to not be a limiting bound, the maximum of the Zhao β parameter and power-law γ_j was increased to allow for steeper slopes, which could present itself as a result of (tidal) truncation. For the same reason, it was removed the smoothness criterion on consecutive power-law slopes, by setting the maximum difference between

Prior	**Minimum**	**Maximum**
$log_{10}\rho_0[M_\odot\ kpc^{-3}]$	5	15
$log_{10}r_s[kpc]$	-2.5	1.5
$\alpha^{(a)}$	0.5	3
$\beta^{(a)}$	3	9
$\gamma^{(a)}$	0	1.5
$\gamma_i^{(b)}$	0	9
β_0	-1	1
β_{infty}	-1	1
$log_{10}r_0[kpc]$	$log_{10}0.5R_e$	$log_{10}2R_e$
η	1	3

Table 3.1: Limits of the uniform pyGravSphere/emcee priors on the dark- matter parameters. NOTE: $^{(a)}$For NFW model it is fixed $(\alpha, \beta, \gamma) = (1, 3, 1)$. $^{(b)}$For $\gamma_{j+1} \geq \gamma_j$.

consecutive slopes equal to the difference between the prior minimum and maximum. The priors parameters used on pyGravSphere runs are displayed in Table 3.1.

For the MCMC chain, it was used the same setting as Genina et al. (2020): 10^3 walkers, making 2×10^4 steps, from which the first half is discarded as burn-in, using 100 integration points. The remaining chain is analyzed by discarding draws with a χ^2 more than ten times the minimum χ^2 and then drawing 10^5 samples from the remaining draws.

From the created chain, pyGravSphere recovers the density profile, by drawing 500 density profile points, from 1 to 600 *pc*, with a step of 1.2 *pc*. The result for the three runs are displayed in Figure 4.7, with a 68% confidence interval at every radius. The corner plots for the constrained values are shown in A.

Chapter 4.

Results and Discussion

4.1 The nature of Leo T stars

4.1.1 Selecting Leo T Members

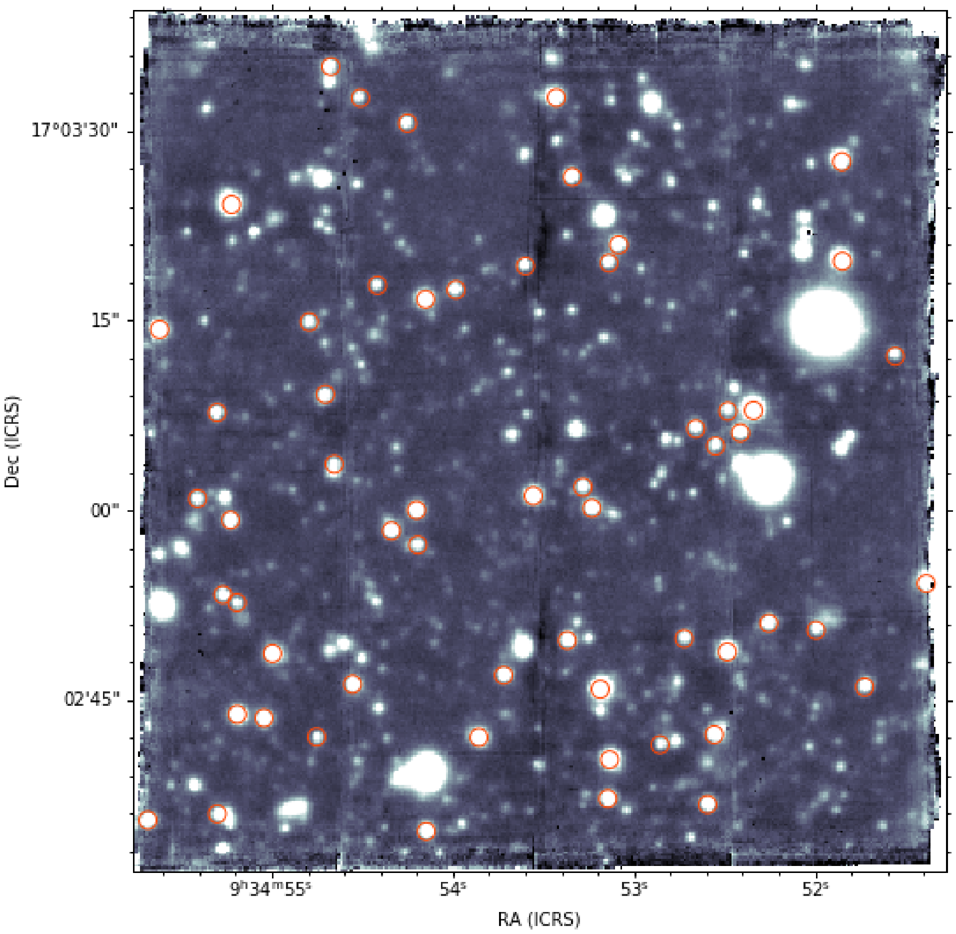

Figure 4.1: White-light image of the final data cube (2.4), with identification of the position for the 58 stars identified as Leo T members. International Celestial Reference System (ICRS) is used to map the position ot the stars.

As discussed in Section 3.1.1, 130 spectra were successful fitted, resulting in, potentially, 130 Leo T member stars. However, even though the fit was flagged successful, many spectra was very noisy. Thus, a cut in S/N was made, by only considering the spectra with $S/N > 3$. As the maximum number of stars is needed in order to allow constraining Leo T density profile, this value was considered as the one that maximizes the number of stars in the sample without affecting the measured velocity dispersion, when comparing with more aggressive cuts. In addition, after plotting the photometric data of the remaining stars in a color-magnitude diagram, one star stood out, as it was much more red than the others.

Hence, 58 stars were considered as plausible members of Leo T, and were used for further analysis.

4.1.2 Ages of Leo T stars

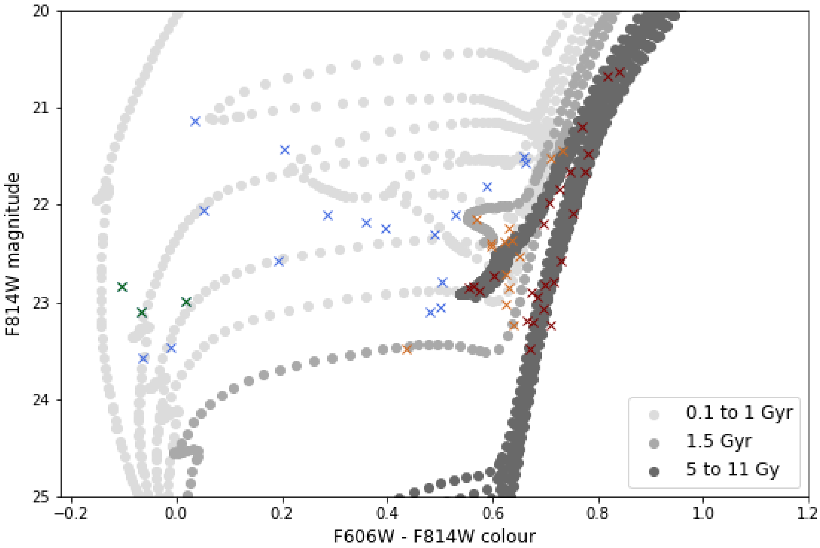

Figure 4.2: Color-magnitude diagram of the 58 Leo T stars detected with MUSE. PARSEC isochrones for a constant $[Fe/H] = -1.6$ are plotted in three shades of grey, pointing out different stellar ages. The stars are marked by crosses of different colors, corresponding to different ages: Stars marked in red are consistent with the older isochrone, blue one are consistent whit younger isochrones, while the orange are consistent with the $1.5 Gyr$ isochrone. It is also highlighted in green three stars, referring to the 3 emission line stars discussed in 4.1.3.

In Figure 4.2 is displayed a color-magnitude diagram for the 58 Leo T stars, plotted against the PARSEC stellar tracks and isochrones mentioned in Section 3.2. The stars are marked as crosses of different colors to reflect for the most consistent isochrone. Thus, red crosses correspond to older stars, while blue crosses correspond to younger stars. Stars consistent with the 1.5Gyr isochrone are displayed in orange. Three stars are marked in green as they were identified as emission line stars.

It is possible to draw several conclusions from this plot. First, all stars are consistent with a metallicity of $[Fe/H] = -1.6$, which was expected from the existent literature. The sample covers a wide range of ages, with stars consistent with a very old ages $>$ 10 billion years, while others appear to be very young, with ages of about 200 million years, or younger. There is also evidence that stars are in different stages of their evolution. The overall consensus on metallicity shows that metallicity evolution on Leo T is almost no existent, which is also verified by the spectroscopic results (see Section 4.1.4) and by the existing literature.

In fact, 20 stars are consistent with ages below one billion years, which confirms that Leo T had star formation in its recent history. An example of young stars are the three stars marked with green crosses, which were identified as emission line stars and are discussed in Section 4.1.3. This proves that Leo T is, indeed, the first UFD with evidence of recent star formation.

4.1.3 Discovery of 3 emission line stars

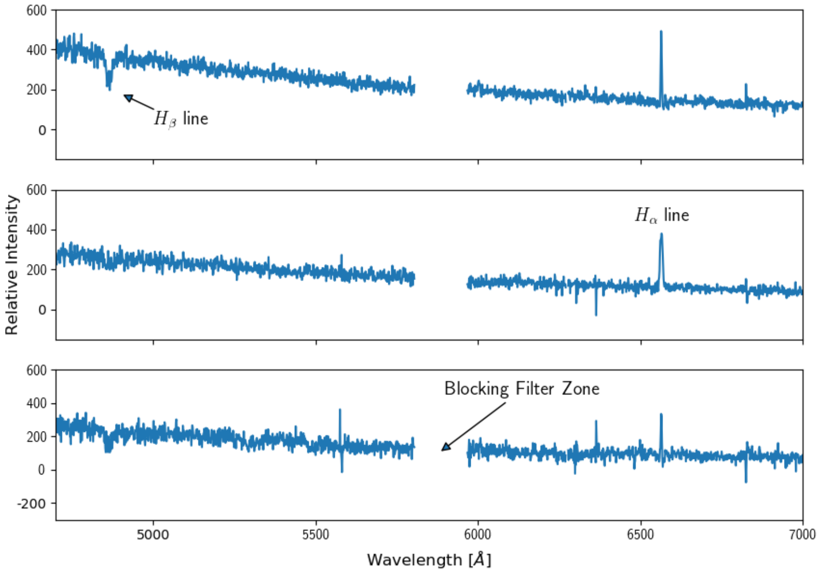

Figure 4.3: Spectra of the 3 mission lines stars. It is pointed out the H_β absorption line and the H_α emission line. It is also visible the zone filtered in order to remove the light from the laser-guide star system.

The stars marked with green crosses in Figure 4.2 stand out for their youth but also for their spectra. In Figure 4.3 is displayed the spectra of these three stars, were is visible that they are emission line stars. In this case, the $H\alpha$ line, instead of being absorption, as normal, it is emission.

Due to their peculiar spectra, spexxy was not able to successfully output fit results. Therefore, these stars were fitted using the *ULySS* code described in Section 3.1.1. They were interpreted as Be stars, which is a set of stars with B spectral type but emission lines. This corresponds to giant stars, with estimated effective temperature of $\sim 10000K$. It was also possible to fit for line-of-sight velocity, and they were used in Leo T dynamics analyze discussed in Section 4.2.

It is relevant to note that these three stars correspond to the first detection ever of emission line stars for an Ultra-Faint Dwarf galaxy.

4.1.4 Metallicity

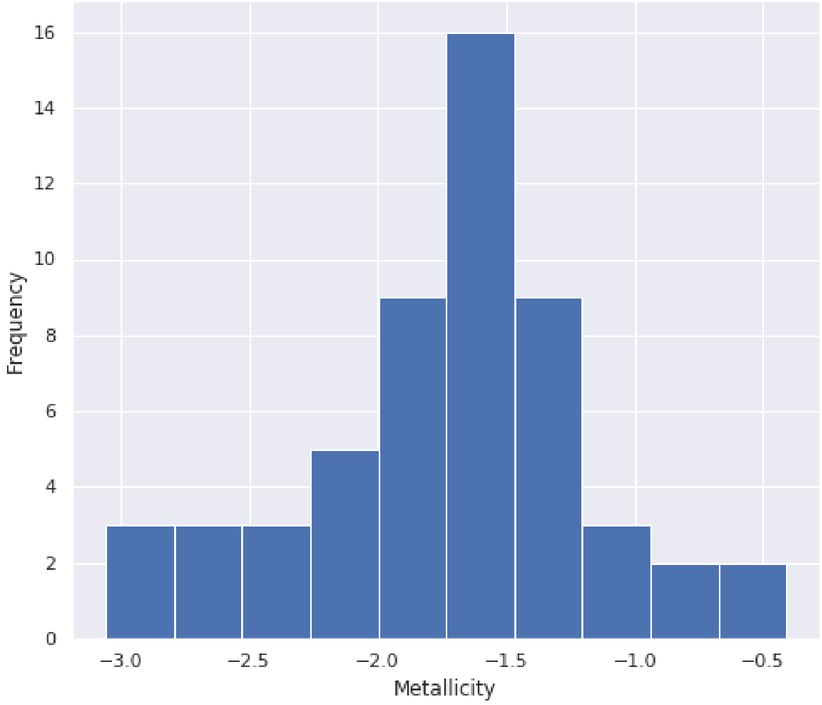

Figure 4.4: Histogram of the metallicity for Leo T members (55 stars), measured by fitting spectra with spexxy.

From the 58 stars identified as Leo T members, spexxy successfully fitted the metallicity for 55 stars, leaving out the three emission line stars. In Figure 4.4 is displayed the histogram of the metallicity using the results for those 55 stars. Using the MCMC method described in Section 3.1.2, the data was fitted using a normal distribution, resulting in a mean value of $[Fe/H] = -1.53^{+0.04}_{-0.05}$, a dispersion of $\sigma_{[Fe/H]} = 0.21 \pm 0.06$, with 99% of the sample being consistent with the model (the corner plot for these results is displayed in A). This results are both consistent with the photometric analysis and with the information available in the literature. The low dispersion is also an indication that this galaxy underwent almost no evolution, as expected.

These results constitute the first metallicity measurement made for Leo T using spectrometric data that is consistent with measurements from photometric analyzes. Nevertheless, spectra metallicity fitting is very dependent on the correct fit for log g and temperature of the stars. This proven itself a very difficult task. Early versions of spexxy failed to fit Leo T spectra for log g. Only after the very recent spexxy update for version 2.5, it was possible to obtain robust measurements of the metallicity of Leo T stars. The aforementioned accordance of these results with the literature consensus about the metallicity of Leo T is assuring of the quality of the spectra obtained with MUSE, and invite to a more complete analysis of Leo T dynamics and inner density.

4.2 Leo T dynamics

As discussed in Section 3.1, it was possible to successfully fit the kinematics for all 58 stars, as the three emission line stars were fitted for these parameter with *ULySS* code. The results from *ULySS* were also used as an independent validation of the spexxy results. To this end, in Figure 4.5 is displayed the plot of the differences between the result of both fits against the measured Signal-to-Noise ratio (SNR) logarithm, for 55 stars (without the emission-line stars). In red is

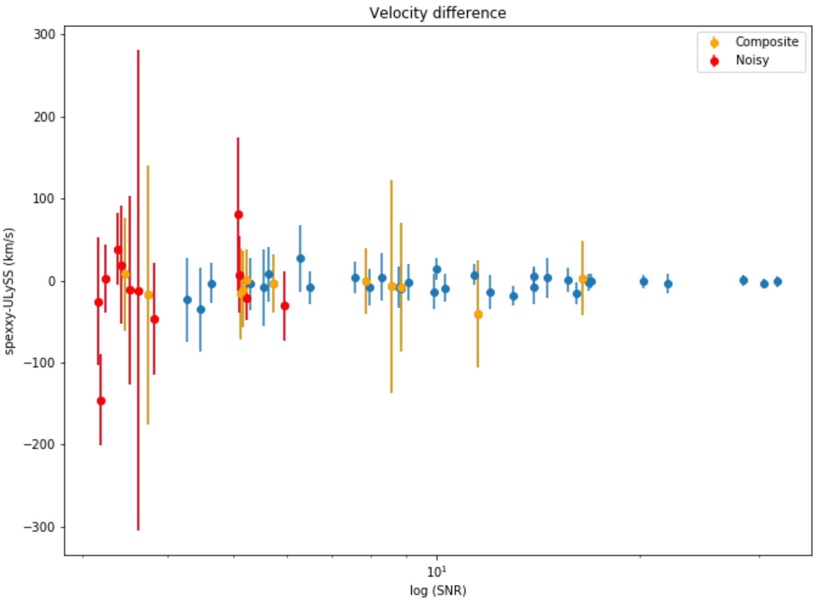

Figure 4.5: Plot of the difference between *spexxy* and *ULySS* velocity estimations, as function of Signal-to-Noise ratio (SNR) logarithm. The displayed error was determined by summing error estimations of both fits. In red is marked the stars flagged as to noisy by *ULySS*, and in orange are displayed the stars that were fitted using multiple reference spectra.

marked the stars considered as to noisy for *ULySS* to be able to make a robust measurement. In orange are displayed the stars that were fitted using multiple reference spectra. These are stars that *ULySS* was not able to derive their spectral type with confidence. The occurrence of this for high signal-to-noise spectra could be a indication that it is a composite spectrum, e.g. from a binary. The displayed error was determined by the sum of error estimations of both fits.

From the results, it is clear that both measures are consistent with each other, except for stars identified as noisy or with *ULySS* multiple reference spectra fitting. Assuming that the differences in velocity of both fits follow a normal distribution, it was used the MCMC method described in Section 3.1.2, to fit the distribution. It was obtained a mean value of $v_{spexxy} - v_{ULySS} = -2.74^{+2.32}_{-2.33}$, a dispersion of $\sigma = 2.28^{+2.43}_{-1.63}$, with 98% of the sample being consistent with the model (the corner plot for these results is displayed in A). This close agreement between both fits shows the solidity of spexxy estimations. There is, however, an indication that spexxy underestimates the velocity (and velocity errors), but this is negligible. The indication of the presence of binary contamination (5 spectra meet the criteria discussed above) is something that was expected. Even though the presence of binaries in UFDs it is still not a very well studied subject, in most cases, stellar velocity dispersion of ultra-faint dwarfs are proven robust against systematic uncertainties such as binary stars and foreground contamination (Simon, 2019).

In order to maximize the sample for the kinematic analysis, data from 17 of the 19 stars (as two are duplicated by MUSE) with kinematics measurements from Simon and Geha (2007) were also used, increasing the sample to 75 stars. The velocity histogram for these 75 stars is displayed in Figure 4.6. Again, the data was fitted using a normal distribution, resulting in a mean value of $v_{los} = 39.37^{+1.30}_{-1.35}\ km\ s^{-1}$, a velocity dispersion of $\sigma_v = 6.98^{+1.32}_{-1.13}\ km\ s^{-1}$ with 99% of the sample being consistent with the model (the corner plot for these results is displayed in A). This values are consistent with the measurements made by Simon and Geha (2007).

For further analysis on how Leo T stars kinematics changes with their age, the first sample, of 58 stars, was divided in two sets: one with the 20 stars consistent with ages $\leq$ 1 billion years, and another with 38 stars consistent with ages $\geq$ 1 billion years. Once again, both sets were fitted with the same MCMC method described above. For the younger sample we have a mean value of $v_{los} = 39.30^{+2.02}_{-2.06}\ km\ s^{-1}$, a velocity dispersion of $\sigma_v = 2.50^{+2.88}_{-1.76}\ km\ s^{-1}$, with 97% of the sample being consistent with the model. For the older sample we got a mean value of $v_{los} = 42.91^{+2.29}_{-2.25}\ km\ s^{-1}$, a velocity dispersion of $\sigma_v = 8.03^{+3.52}_{-2.85}\ km\ s^{-1}$, with 98% of the sample being consistent with the model (the corner plot for these results is displayed in A).

These results show that younger stars have much less velocity dispersion, while having a smaller mean velocity. This very similar to what was found by Adams and Oosterloo (2018), when analyzing the HI kinematics. This confirms that both gas and star kinematics are in agreement, and these results are the first evidence that young Leo T stars have kinematics similar to the cold component of the gas. This is something that was predicted by Simon and Geha (2007), as of the first evidence that the gas of Leo T is accurately tracing the gravitational potential of the galaxy. This is particular interesting as, if this result also applies to other dwarfs, then HI kinematics can be used to measure the galaxy masses reliably.

In order to analyze the kinematics variation with the radius, the sample of 75 stars were divided in four bins, according to their distant to the center of Leo T. Each bin was fitted using the MCMC method, but no significant results were found, as the kinematics appears to be constant disregarding the radius. However, because $\sim$ 90% of the stars in the sample are within the half-light radius, there are not sufficient probes at outer radii to be possible to have a definite conclusion. Furthermore, as the velocity dispersion calculated here appears to be smaller than others available studies that cover a much wider are, it is plausible that the velocity dispersion increases with radii.

Using Equation 1.3 and the estimated σ_v for the sample of 75 stars, it was estimated the mass at the half-light radius $M_{1/2} = 5.07^{+2.06}_{-1.53} \times 10^6\ M_\odot$. This equation was also used to measure the mass within each one of the four bins aforementioned, that was used to make a more simple measure of the density at four points of Leo T galaxy radius. This results are plotted, as red dots, in Figure 4.7, along with pyGravSphere density profiles.

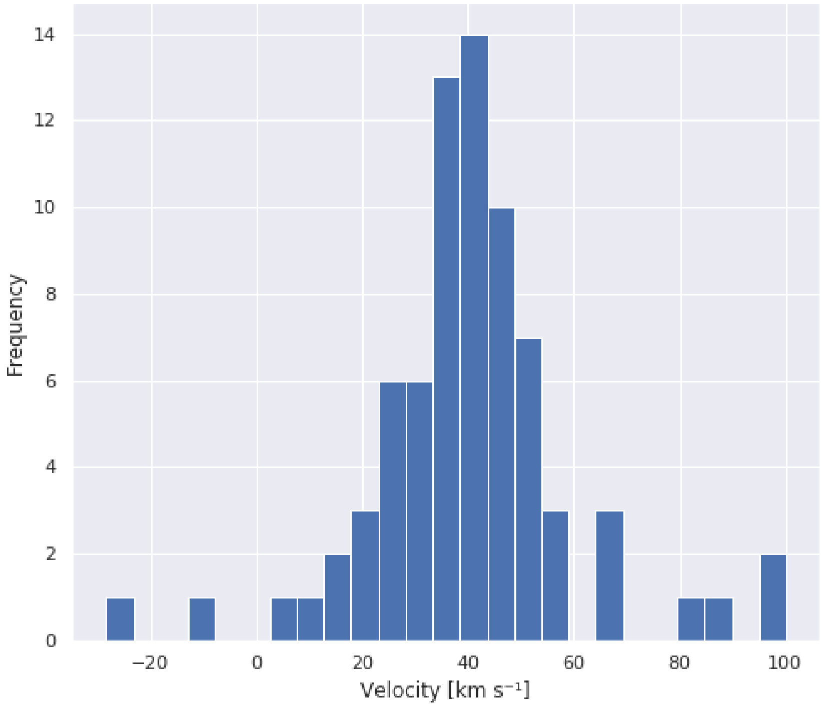

Figure 4.6: Histogram of the velocity for Leo T members (75 stars), measured by fitting its spectra with spexxy (55 stars), ULySS (3 stars) and by Simon and Geha (2007) (17 stars).

4.3 Density Profiles

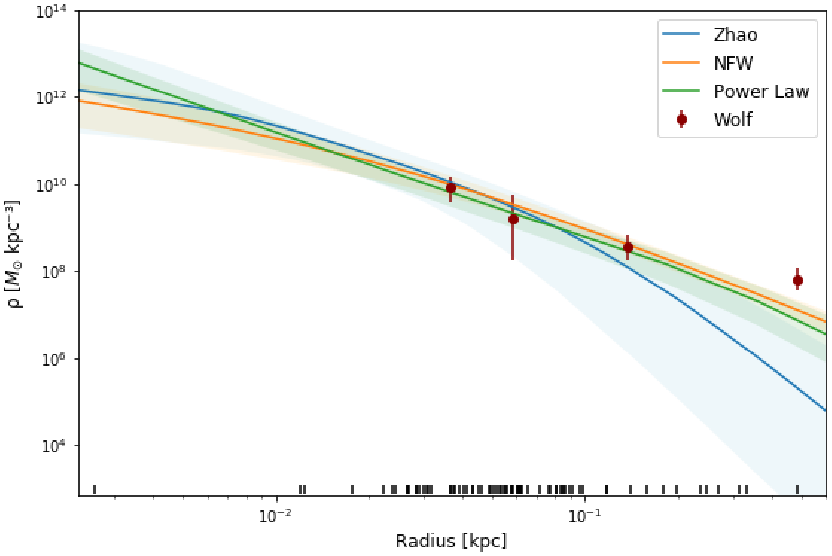

Figure 4.7: Density profiles using 3 different models, with a 68% confidence interval at every radius.The dashes at the plot bottom trace the position of the stars. It is also plotted density estimations using Wolf et al. (2010) mass estimator.

The holy grail for dark matter research in dwarf galaxies is the conclusive measurement of the inner density profile of a highly dark matter-dominated system. The disadvantage of trying to do this with an UFD is that it is very difficult to gather enough dynamical tracers for a robust measurement of the mass distribution. A sample of 75 stars should be sufficient for the task, however a larger sample may be needed to distinguish a central dark matter cusp from a core, if the core of Leo T is not fairly large. Thus, following the analyze described in Section 3.3, it was possible to derive the first ever dark matter density profile of Leo T.

The results are displayed in Figure 4.7. Are shown three different density profiles, with a 68% confidence interval at every radius. As discussed in Section 3.3, it was used a Power Law model (eq. 3.4), Zhao model (eq. 3.5) and NFW model (eq. 1.1). The dashes at the bottom of the plot trace the star positions.

Plotted in the same graph, marked as red dots, are the results of the more trivial density estimations, done by using Equation 1.3 for different radii values. This equation was used to estimate the mass of each one of the four bins mentioned in the previous section and, dividing by the bin volume, estimate the density of each bin.

The three profiles, agree very well with each other, specially at more populated radius. The results of the more trivial density analysis are also in agreement with the density profiles resulting from pyGravSphere analysis, specially at inner radius. This is reassuring that the system is fairly simple in its dynamical structure. These profiles are rather more consistent with a profile expected from cold dark matter models, than the ones observed for more massive dwarfs. In fact, there is no evidence of a core, as the profiles resembles more a cusp.

This is in agreement with predictions from (Bullock and Boylan-Kolchin, 2017) and consistent with the results of Figures 1.2 and 1.3. Assuming that a core is created by the action of stellar winds or supernovae feedback and that the effect of core creation will vary with the number of stars formed, Leo T stellar mass would not be sufficient to create a core. Even though the number of stars in the sample is not large enough to give a entirely conclusive measurement of the inner density profile of this dwarf, these results favors the hypothetical *cusp-core* problem solution that the effect of core creation will vary with the galaxy stellar mass.

These results are very promising and future spectroscopic observations of Leo T can increase the sample of stars with measure kinematics and, by combining radial velocities and proper motions, it is possible to provide much more accurate measurements of the density profile of the dwarf.

4.4 Bounds on ALP Dark Matter

As mentioned, the data cube described in Section 2.3.10 was used to search for DM in Leo T, in the form of **A**xion-**L**ike **P**articles (ALPs) by exploiting their coupling to photons, whose results were published in a paper by Regis, Taoso, Vaz et al. (2020). The strategy used was to look for the monochromatic photon flux generated by ALP decays. As the data cube covers wavelengths in the range of $470 - 935$ nm it was possible to search for ALPs signals from the Leo T for masses between 2.7 and 5.3 eV.

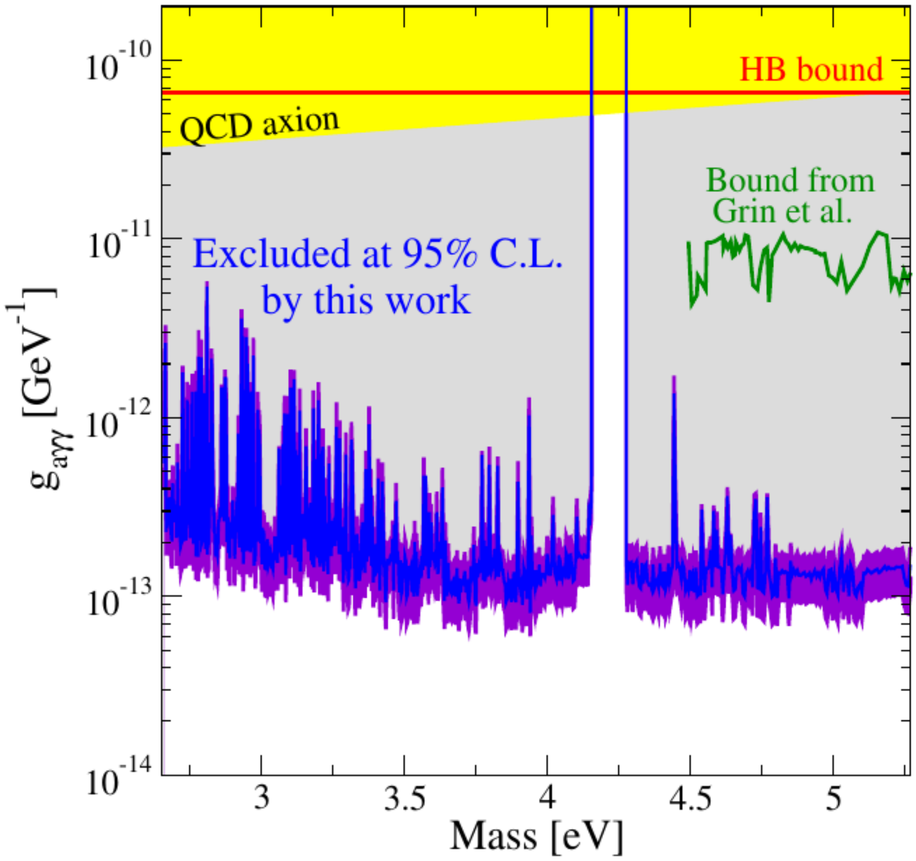

Figure 4.8: The solid blue curve shows the 95% C.L. upper limits on the effective ALP-two-photon coupling $g_{a\gamma\gamma}$ as a function of the ALP mass. The violet area includes the uncertainties on the D-factor. In green it is shown the bound derived from observation of clusters, in red the bound derived from the ratio of horizontal branch (HB) to red giants stars in globular clusters, and in yellow the preferred region for the QCD axion (Source: Regis et al. (2020)).

The results obtained are shown in Figure 4.8. The curves show rapid variation at lower energies/longer wavelengths, reflecting the presence of strong OH emission lines from the night sky which increases the noise here. These results improve existing bounds by more than one order of magnitude. For the complete study see Regis et al. (2020).

Chapter 5.

Conclusions

In this task of analyzing Leo T UFD nature, the main obstacle was to gather a large enough sample to be able to complete the proposed objectives. MUSE spectrograph proved to be a fundamental weapon to this end, as it allowed to increase the number of spectroscopically observed Leo T stars from 19 to 75. Even though this is not a huge sample, it was possible to obtain very interesting results.

It was identified a wide range of stellar ages, with stars younger than $\sim 200\ Myr$. Within those, it was discovered three Be emission line stars, the first discovered for an Ultra-Faint Dwarf. The existence of such young stars also testify that Leo T underwent through star formation very recently, being the only UFD for which this was observed.

By fitting the spectra, it was estimated a metallicity of $[Fe/H] = -1.53^{+0.04}_{-0.05}$, in total agreement with the expectation. This is the first spectrometric study of Leo T metallicity with results consistent with the photometric studies available. A metallicity dispersion of $\sigma_{[Fe/H]} = 0.21 \pm 0.06$ indicates that Leo T underwent almost no evolution throughout its history, which is expected for an UFD.

The kinematics of Leo T stars were measured, in the most robust kinematic study of the dwarf until date. It was measured a velocity dispersion of $\sigma_v = 6.98^{+1.32}_{-1.13}\ km\ s^{-1}$, which is consistent with previous estimations of stars and HI gas kinematics. There is also evidence that the kinematic of younger stars are in agreement with the kinematics of the gas cold component. This indicates that recent star formation occurred within bubbles of cold gas, as would be expected. Using this results it was estimated the mass within the half-light radius $M_{1/2} = 5.07^{+2.06}_{-1.53} \times 10^6\ M_{\odot}$.

The kinematics study led to the first derived Dark Matter profile for this dwarf. The resulting profile does not appear to show a core, like other more massive dwarfs. This is predicted by a possible solution of the $cusp - core$ problem. Assuming that a core is created by the action of stellar winds or supernovae feedback and that the effect of core creation will vary with the number of stars formed, Leo T stellar mass would not be sufficient to create a core. Nevertheless, the number of stars in the sample is not large enough to give a entirely conclusive measurement of the inner density profile of this dwarf. However, it is quite promising.

MUSE data of Leo T was also used to search for DM in the form of ALPs. It was possible to derive new bounds on the effective ALP-two-photon couplings, which improve existing constraints from observations of clusters and stars in globular clusters by more than one order of magnitude. These results, that were published in a paper by Regis et al. (2020), show that additional UFDs observations with MUSE will allow to improve current exclusion limits and, possibly, provide a detection of ALP signal.

In this sense, further observations of Ultra-Faint dwarfs would be key for constraining the nature of dark matter and to improve the knowledge of the galaxy formation process. MUSE spectrograph proved to be a great ally in the observation of these objects, and expanding the number of UFDs observed with it, and with next generation instruments, will certainly bring exciting results.

Bibliography

Adams, E. A. K. and T. A. Oosterloo (2018). “Deep neutral hydrogen observations of Leo T with the Westerbork Synthesis Radio Telescope”. In: *Astronomy & Astrophysics* 612, A26. ISSN: 1432-0746. DOI: 10.1051/0004-6361/201732017. URL: http://dx.doi.org/10.1051/0004-6361/201732017.

Bacon, R. et al. (2010). “The MUSE second-generation VLT instrument”. In: *Ground-based and Airborne Instrumentation for Astronomy III*. Ed. by I. S. McLean, S. K. Ramsay, and H. Takami. Vol. 7735. International Society for Optics and Photonics. SPIE, pp. 131 –139. DOI: 10.1117/12.856027. URL: https://doi.org/10.1117/12.856027.

Bacon, R. et al. (2017). “The MUSE Hubble Ultra Deep Field Survey”. In: *Astronomy & Astrophysics* 608, A1. ISSN: 1432-0746. DOI: 10.1051/0004-6361/201730833. URL: http://dx.doi.org/10.1051/0004-6361/201730833.

Baes, M. and E. Van Hese (2007). “Dynamical models with a general anisotropy profile”. In: *Astronomy & Astrophysics* 471(2), 419–432. ISSN: 1432-0746. DOI: 10.1051/0004-6361:20077672. URL: http://dx.doi.org/10.1051/0004-6361:20077672.

Bertin, E. and S. Arnouts (1996). “SExtractor: Software for source extraction”. In: *Astronomy & Astrophysics Supplement Series* 117, pp. 393–404.

Bressan, A. et al. (2012). “parsec: stellar tracks and isochrones with the PAdova and TRieste Stellar Evolution Code”. In: *Monthly Notices of the Royal Astronomical Society* 427(1), 127–145. ISSN: 1365-2966. DOI: 10.1111/j.1365-2966.2012.21948.x. URL: http://dx.doi.org/10.1111/j.1365-2966.2012.21948.x.

Bullock, J. S. and M. Boylan-Kolchin (2017). “Small-Scale Challenges to the ΛCDM Paradigm”. In: *Annual Review of Astronomy and Astrophysics* 55(1), 343–387. ISSN: 1545-4282. DOI: 10.1146/annurev-astro-091916-055313. URL: http://dx.doi.org/10.1146/annurev-astro-091916-055313.

Clementini, G. et al. (2012). “VARIABILITY AND STAR FORMATION IN LEO T, THE LOWEST LUMINOSITY STAR-FORMING GALAXY KNOWN TODAY”. In: *The Astrophysical Journal* 756(2), p. 108. ISSN: 1538-4357. DOI: 10.1088/0004-637x/756/2/108. URL: http://dx.doi.org/10.1088/0004-637X/756/2/108.

Foreman-Mackey, D. (June 2016). “corner.py: Scatterplot matrices in Python”. In: *The Journal of Open Source Software* 1. DOI: 10.21105/joss.00024.

Foreman-Mackey, D. et al. (2013). “emcee: The MCMC Hammer”. In: *Publications of the Astronomical Society of the Pacific* 125(925), 306–312. ISSN: 1538-3873. DOI: 10.1086/670067. URL: http://dx.doi.org/10.1086/670067.

Genina, A et al. (2020). “To β or not to β: can higher order Jeans analysis break the mass–anisotropy degeneracy in simulated dwarfs?” In: *Monthly Notices of the Royal Astronomical Society* 498(1), 144–163. ISSN: 1365-2966. DOI: 10.1093/mnras/staa2352. URL: http://dx.doi.org/10.1093/mnras/staa2352.

Hinton, S. et al. (2016). “Marz: Manual and automatic redshifting software”. In: *Astronomy and Computing* 15, 61–71. ISSN: 2213-1337. DOI: 10.1016/j.ascom.2016.03.001. URL: http://dx.doi.org/10.1016/j.ascom.2016.03.001.

Husser, T.-O. et al. (2013). “A new extensive library of PHOENIX stellar atmospheres and synthetic spectra”. In: *Astronomy & Astrophysics* 553, A6. ISSN: 1432-0746. DOI: 10.1051/0004-6361/201219058. URL: http://dx.doi.org/10.1051/0004-6361/201219058.

Husser, T.-O. (2012). *3D-Spectroscopy of Dense Stellar Populations*. Universitätsverlag Göttingen: Göttingen. DOI: 10.17875/gup2012-87.

Irwin, M. J. et al. (2007). “Discovery of an Unusual Dwarf Galaxy in the Outskirts of the Milky Way”. In: *The Astrophysical Journal* 656(1), L13–L16. ISSN: 1538-4357. DOI: 10.1086/512183. URL: http://dx.doi.org/10.1086/512183.

Jong, J. T. A. de et al. (2008). “The Structural Properties and Star Formation History of Leo T from Deep LBT Photometry”. In: *The Astrophysical Journal* 680(2), 1112–1119. ISSN: 1538-4357. DOI: 10.1086/587835. URL: http://dx.doi.org/10.1086/587835.

Kamann, S., L. Wisotzki, and M. M. Roth (2012). “Resolving stellar populations with crowded field 3D spectroscopy”. In: *Astronomy & Astrophysics* 549, A71. ISSN: 1432-0746. DOI: 10.1051/0004-6361/201220476. URL: http://dx.doi.org/10.1051/0004-6361/201220476.

Kirby, E. N. et al. (2013). “THE UNIVERSAL STELLAR MASS-STELLAR METALLICITY RELATION FOR DWARF GALAXIES”. In: *The Astrophysical Journal* 779(2), p. 102. ISSN: 1538-4357. DOI: 10.1088/0004-637x/779/2/102. URL: http://dx.doi.org/10.1088/0004-637X/779/2/102.

Kroupa, P. (2001). “On the variation of the initial mass function”. In: *Monthly Notices of the Royal Astronomical Society* 322(2), 231–246. ISSN: 1365-2966. DOI: 10.1046/j.1365-8711.2001.04022.x. URL: http://dx.doi.org/10.1046/j.1365-8711.2001.04022.x.

Mateo, M. L. (Jan. 1998). “Dwarf Galaxies of the Local Group”. In: *Annual Review of Astronomy and Astrophysics* 36, pp. 435–506. DOI: 10.1146/annurev.astro.36.1.435. arXiv: astro-ph/9810070 [astro-ph].

Navarro, J. F., C. S. Frenk, and S. D. M. White (1997). “A Universal Density Profile from Hierarchical Clustering”. In: *The Astrophysical Journal* 490(2), 493–508. ISSN: 1538-4357. DOI: 10.1086/304888. URL: http://dx.doi.org/10.1086/304888.

Piqueras, L. et al. (Oct. 2017). “MPDAF - A Python package for the analysis of VLT/-MUSE data”. In: *arXiv e-prints*, arXiv:1710.03554, arXiv:1710.03554. arXiv: 1710.03554 [astro-ph.IM].

Plummer, H. C. (Mar. 1911). “On the Problem of Distribution in Globular Star Clusters: (Plate 8.)” In: *Monthly Notices of the Royal Astronomical Society* 71(5), pp. 460–470. ISSN: 0035-8711. DOI: 10.1093/mnras/71.5.460. eprint: https://academic.oup.com/mnras/article-pdf/71/5/460/2937497/mnras71-0460.pdf. URL: https://doi.org/10.1093/mnras/71.5.460.

Read, J. I. and P. Steger (2017). “How to break the density-anisotropy degeneracy in spherical stellar systems”. In: *Monthly Notices of the Royal Astronomical Society* 471(4), 4541–4558. ISSN: 1365-2966. DOI: 10.1093/mnras/stx1798. URL: http://dx.doi.org/10.1093/mnras/stx1798.

Read, J. I., M. G. Walker, and P Steger (2019). "Dark matter heats up in dwarf galaxies". In: *Monthly Notices of the Royal Astronomical Society* 484(1), 1401–1420. ISSN: 1365-2966. DOI: 10.1093/mnras/sty3404. URL: http://dx.doi.org/10.1093/mnras/sty3404.

Regis, M. et al. (2020). *Searching for Light in the Darkness: Bounds on ALP Dark Matter with the optical MUSE-Faint survey.* arXiv: 2009.01310 [astro-ph.CO].

Richard, J., R. Bacon, and J. Vernet (2019). *MUSE User Manual.* ESO-261650, v10.4. ESO.

Roth, Martin M. et al. (2018). "MUSE crowded field 3D spectroscopy in NGC 300 - I. First results from central fields". In: *A&A* 618, A3. DOI: 10.1051/0004-6361/201833007. URL: https://doi.org/10.1051/0004-6361/201833007.

Ryan-Weber, E. V. et al. (2008). "The Local Group dwarf Leo T: HI on the brink of star formation". In: *Monthly Notices of the Royal Astronomical Society* 384(2), 535–540. ISSN: 1365-2966. DOI: 10.1111/j.1365-2966.2007.12734.x. URL: http://dx.doi.org/10.1111/j.1365-2966.2007.12734.x.

Simon, J. D. (2019). "The Faintest Dwarf Galaxies". In: *Annual Review of Astronomy and Astrophysics* 57(1), 375–415. ISSN: 1545-4282. DOI: 10.1146/annurev-astro-091918-104453. URL: http://dx.doi.org/10.1146/annurev-astro-091918-104453.

Simon, J. D. and M. Geha (2007). "The Kinematics of the Ultra-faint Milky Way Satellites: Solving the Missing Satellite Problem". In: *The Astrophysical Journal* 670(1), 313–331. ISSN: 1538-4357. DOI: 10.1086/521816. URL: http://dx.doi.org/10.1086/521816.

Weilbacher, P. M. et al. (2012). "Design and capabilities of the MUSE data reduction software and pipeline". In: *Software and Cyberinfrastructure for Astronomy II.* Ed. by N. M. Radziwill and G. Chiozzi. Vol. 8451. International Society for Optics and Photonics. SPIE, pp. 102 – 110. DOI: 10.1117/12.925114. URL: https://doi.org/10.1117/12.925114.

Weilbacher, P. M. et al. (2020). *The Data Processing Pipeline for the MUSE Instrument.* arXiv: 2006.08638 [astro-ph.IM].

Weisz, D. R. et al. (2012). "THE STAR FORMATION HISTORY OF LEO T FROM HUBBLE SPACE TELESCOPE IMAGING". In: *The Astrophysical Journal* 748(2), p. 88. ISSN: 1538-4357. DOI: 10.1088/0004-637x/748/2/88. URL: http://dx.doi.org/10.1088/0004-637X/748/2/88.

Wolf, J. et al. (2010). “Accurate masses for dispersion-supported galaxies”. In: *Monthly Notices of the Royal Astronomical Society*, no–no. ISSN: 1365-2966. DOI: `10.1111/j.1365-2966.2010.16753.x`. URL: `http://dx.doi.org/10.1111/j.1365-2966.2010.16753.x`.

Zhao, H. (1996). “Analytical models for galactic nuclei”. In: *Monthly Notices of the Royal Astronomical Society* 278(2), 488–496. ISSN: 1365-2966. DOI: `10.1093/mnras/278.2.488`. URL: `http://dx.doi.org/10.1093/mnras/278.2.488`.

Zoutendijk, S. L. et al. (Mar. 2020). “The MUSE-Faint survey”. In: *Astronomy & Astrophysics* 635, A107. ISSN: 1432-0746. DOI: `10.1051/0004-6361/201936155`. URL: `http://dx.doi.org/10.1051/0004-6361/201936155`.

Appendices

Chapter A.

Corner Plots

Here are presented the *corner* plots created during the analyzes of the data.

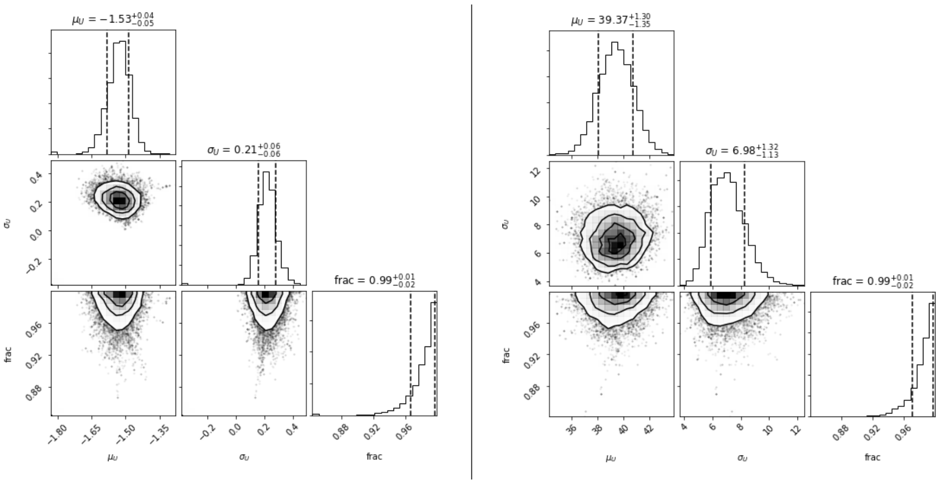

Figure A.1: Corner plot for the MCMC metallicity fit, using a sample of 55 stars (left) and for the MCMC velocity fit, using the entire sample of 75 stars (right). It is displayed the mean value μ_u, dispersion σ_u and fraction of stars consistent with the model.

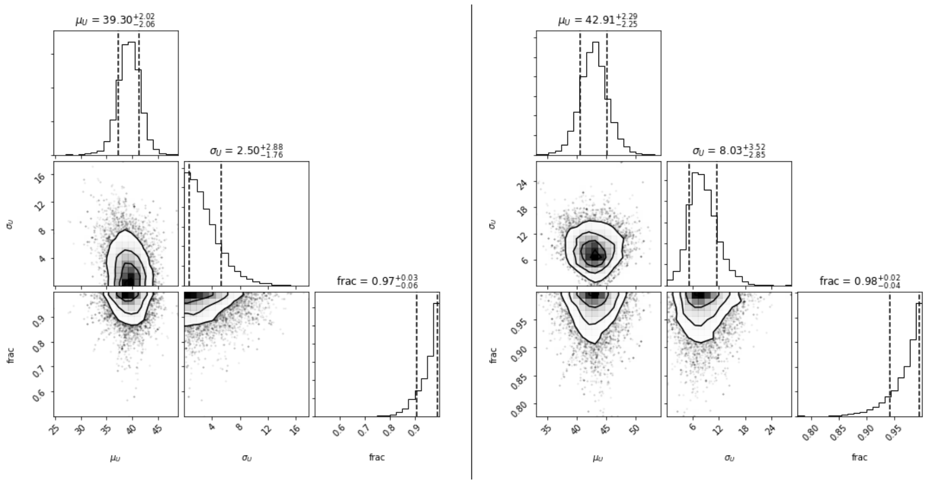

Figure A.2: Corner plot for the MCMC velocity fit, using a sample of 20 young stars (left) and a sample of 38 stars (right). It is displayed the mean value μ_u, dispersion σ_u and fraction of stars consistent with the model.

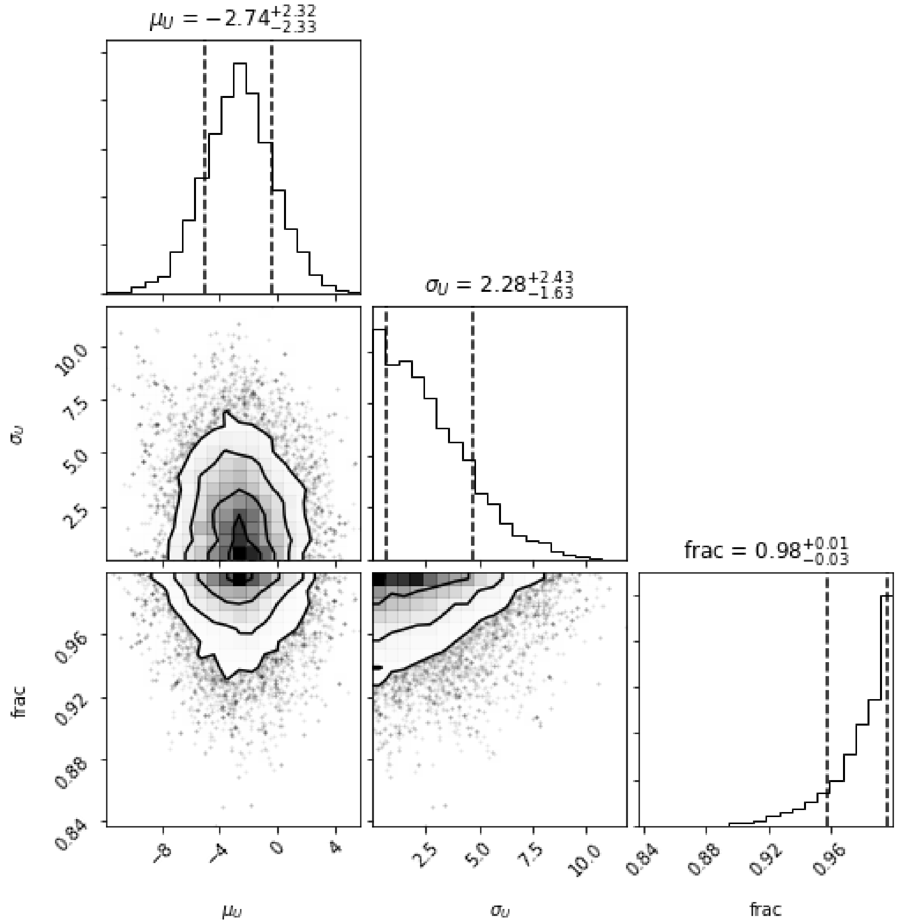

Figure A.3: Corner plot for the velocity difference between spexxy and *ULySS* fits, using a sample of 55 stars. It is displayed the mean value μ_u, dispersion σ_u and fraction of stars consistent with the model.

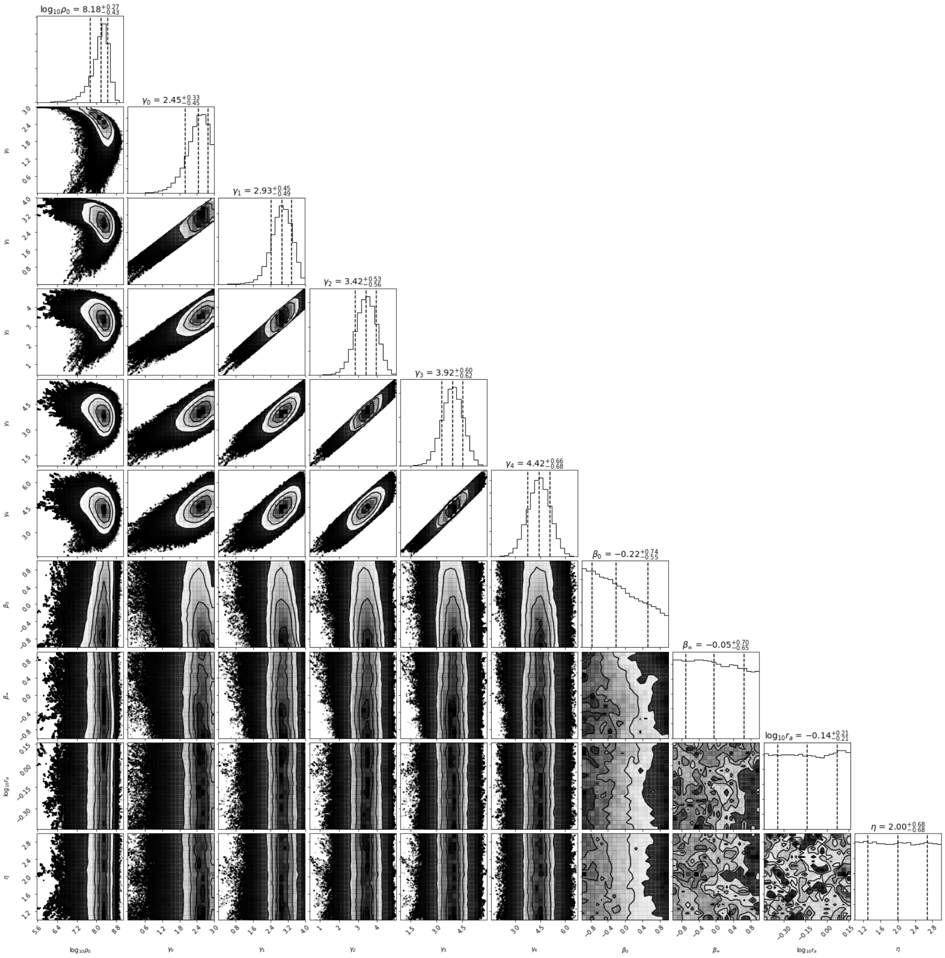

Figure A.4: Corner plot for pyGravSphere run for the Power Law Profile.

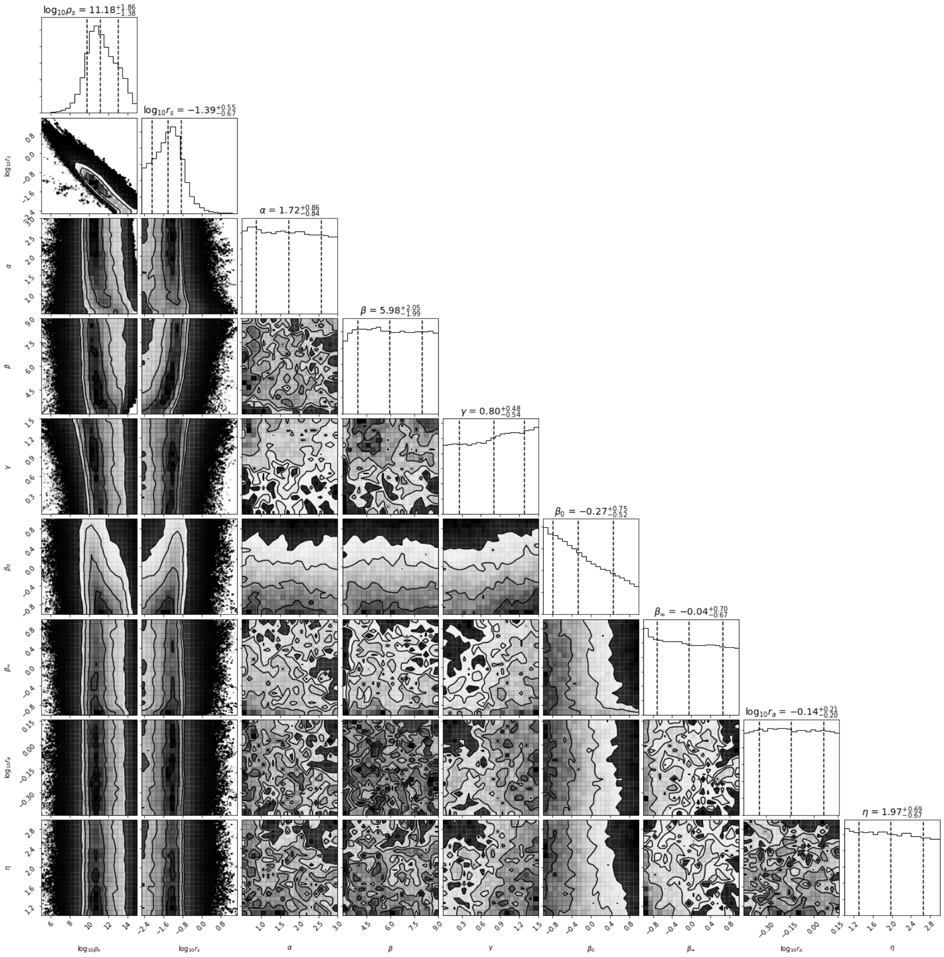

Figure A.5: Corner plot for pyGravSphere run for the Zhao Profile.

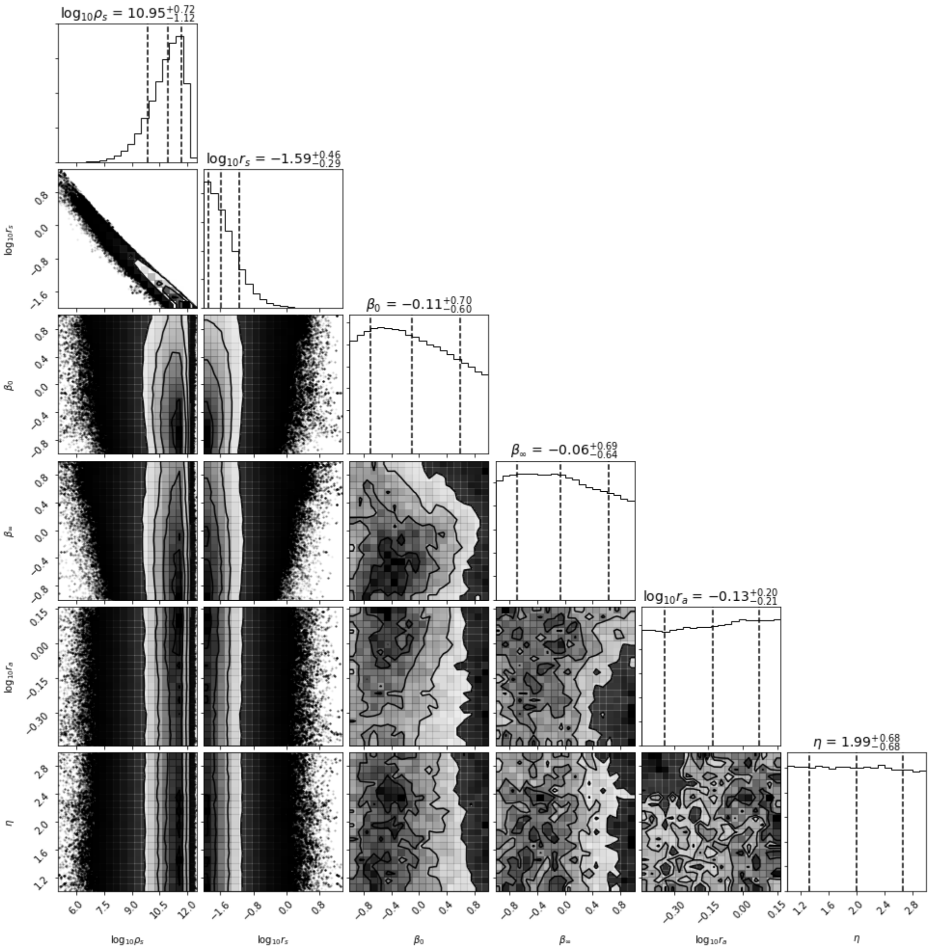

Figure A.6: Corner plot for pyGravSphere run for the NFW Profile.